Quasiparticle Coherence in a Quenched Mott State

Nicolas Jacquier,
under supervision of Mrs. Corinna Kollath

Master thesis, Département de physique, Université de Genève, Suisse

June 2012

Chapter 1

Introduction

In 1924, Einstein investigated theoretically the ideal atomic Bose gas with the statistics introduced by Bose the same year for photons. He predicted that, at temperatures close to the absolute zero, the bosons occupy the lowest energy level, where quantum effects can be observed on the macroscopic scale. This state of matter is called the Bose-Einstein condensate (BEC).

Its experimental realization remained a challenge over about seventy years, because temperatures of the order of the nano-Kelvin has to be reached. In 1995, thanks to laser and evaporating cooling techniques, this was achieved with rubidium [1], sodium [12] and lithium [6] atoms. The way was paved for the exploration of quantum phenomena on a macroscopic scale: interference between two condensates [2], collective modes [11], etc. Many-body effects, such as the quantum phase transition between a Mott-insulating and a superfluid state, were revealed experimentally in [20].

In a Bose-Einstein condensate, the interaction energy in usually about 200 lower than the kinetic energy. This weakly interacting regimes are well-described by mean-field theories [42]. However, regimes where the kinetic energy of the atoms is of the order of the interaction energy are even more interesting, because the correlations between the atoms become important. Experimentally, this was achieved: because the bosons mainly interact by s-wave scattering, increasing the s-wave scattering length by Feshbach resonance [42] allows to reach strong coupling regimes. The drawback is a decrease of the lifetime of the atomic cloud [10, 13].

However, experiments performed by M. Greiner and collaborators provided another approach. There, the kinetic energy is lowered, allowing a longer lifetime for the BEC. To do so, the cloud of cold atoms is first loaded into an optical potential (see [5, 19] and references therein), which is an artificial lattice potential created by two counter propagating laser beams. The motion of the bosons is then frozen: they are trapped into the intensity maxima or minima of this light field. They can only move from site to site by tunneling. The tunable height of the optical lattice allows to vary the kinetic energy by several orders of magnitude. A large height is tantamount to a small tunneling probability, and conversely.

Much more stable, the atomic cloud obtained with this method can also be very finely tuned: the parameters in the Hamiltonian are much more controlled. They can be changed almost at will, and measurement of quantities such as the momentum distribution or the parity correlation function [9] can be done with a great precision. Either

a BEC with non-interacting bosons or a strongly interacting atomic cloud can be created and maintained. Depending on the interaction strength, the atomic cloud can be found in two different phases. The properties of both are now well-known, and the phase transition which takes place revealed experimentally [20]. In chapter 2, we present those properties, notably the differences between the superfluid and Mott-insulating phases. We introduce the physical quantities which will be important in the next chapters, the one-body correlation function, and the momentum distribution, because they allow a real understanding of the cold bosons.

In the weakly interacting regime, the atoms show long-range phase coherence and can be described by a macroscopic wavefunction. Thus quantum phenomena can be seen on a macroscopic scale. This phase coherence can be revealed by the momentum distribution [19]. Experimentally accessible by so-called time-of-flight measurement (see section 2.3.1), theoretical studies have to be led numerically, when no approximative analytical methods exist.

For several years a powerful numerical tool in the study of one-dimensional systems on a lattice, called the Density Matrix Renormalization Group (DMRG), has been developed and used extensively on a variety of situation. This work will also use intensively. In chapter 3, we present its essence, and its efficiency to modelize one-dimensional systems.

But the new method of M. Greiner *et al* also opened a whole new area of non-equilibrium phenomena. Quenching, for example, which is a sudden change of a parameter in the Hamiltonian, resulting in the propagation of information with a certain speed. This is studied in chapter 4, where the optical lattice height, initially high, is lowered, so as to facilitate tunneling from site to another. After the quench, propagating quasiparticles are formed of elementary excitations. We try to understand their structure, and to decipher the dynamics the quench induces. In 4.2, we show a coherence exists between the several superpositions of quasiparticles. With the help of a perturbative tool developed in chapter 3, we understand which frequencies are involved in those quasiparticles.

Finally, in chapter 5, the behavior of two different bosonic species in interaction is considered, from both the static and time-dependent points of view. The addition of a second species can modify considerably the ground state properties, introducing new phases. However, we focus on the interaction between a strongly correlated Mott-insulating state and a superfluid, in a range of parameters far from these new and intriguing phases. A quench is performed on the strongly interacting species, towards lower interactions, a situation comparable to the one studied in the previous chapter.

We investigate qualitatively whether the quasiparticle picture, valid in the single-species case, is still applicable, or if the added superfluid invalidate this picture. Our study indicates that the superfluid "dresses" the quasiparticle without destroying it, and increases the coherence of the system.

Contents

Chapter 2

The Physics of Cold Atomic Gases

In this chapter, we start by deriving the Hamiltonian of an atomic cloud in an optical lattice. Within some approximation, a discrete form can be obtained, which is correct provided only the lowest-lying energy band is occupied. Experimentally, this can be ensured by maintaining the typical energies of the system below the gap. This Hamiltonian shows two parameters, one accounting for the interaction, one for the tunneling ("hopping") between the lattice sites. Both are experimentally tunable with great precision, respectively by choosing atoms with different s-wave scattering length and changing the lattice depth (that is, the laser amplitude).

Once this is done, we diagonalize the Bose-Hubbard Hamiltonian obtained in two limiting cases, no interaction, and no hopping. For a particular value of the *filling* factor, which is the number of sites divided by the total number of atoms in the cloud, two phases are found. We then turn to a numerical, approximate diagonalization to explore the properties of this Hamiltonian, such as energy, one-body correlations, etc. The momentum distribution is introduced and its importance in experiments explained.

Finally, a first approach of a non-equilibrium situation is presented as well as the notion of quench, which will be used extensively in chapter 4.

2.1 Static Bose-Hubbard Model on a Lattice

As explained in the introduction, a stable atomic gas in which the interaction and kinetic energies are comparable can be achieved by creating a periodic lattice over the atomic cloud. This lattice hinders the movements of the atoms, which becomes only possible through quantum tunneling. Therefore, the kinetic energy is considerably reduced, to the order of the interaction energy. As compared to the techniques where the interaction energy is increased to the order of the kinetic energy, the system gains in life-time and stability.

By the interference of two counter-propagating laser beams, a so-called optical lattice can be induced, which simulates the desired lattice potential. Via the optical dipole interaction (see [21, 19] for details), the atoms will be located at the intensity minima or maxima of the lasers. A cloud of (bosonic) atoms can thus be ordered into a one-dimensional lattice. Their interaction is repulsive and mostly take place through s-wave scattering theory [24].

In this section, we construct the Hamiltonian of the BEC, and use the fact that we now have a discrete lattice to obtain a discrete formulation, which is the most helpful form.

The most general form is:

$$H = \int d^3x \Psi^\dagger(x) \left(-\frac{\hbar^2}{2m}\nabla^2 + V_{\text{external}}(x) + \frac{2\pi a_s \hbar^2}{m}\Psi^\dagger(x)\Psi(x) \right) \Psi(x), \tag{2.1}$$

where $\Psi(x)$ is the bosonic field operator and $\Psi^\dagger(x)$ its hermitian conjugate. The first term contains the kinetic energy of the atoms and V_{external} all optional external potential, including the lattice potential. m is the mass of the atoms, a_s their s-wave scattering length; these experimental parameters weight the interaction term of the Hamiltonian. In the case of cold bosons, this interaction is on-site and short-range, and therefore well approximated by an isotropic pseudopotential. Once for all we set $\hbar = 1$ and do not repeat it.

The presence of a periodic potential induces an energy band structure, which will be discussed in section 2.2.2. A gap opens between the lowest lying bands, which increases with the lattice depth. Therefore, if a large lattice depth is used, the typical energies involved in the system are smaller than the gap, and the atoms are confined to the lowest band. The Wannier function of the lowest band, w_0, can be used to describe this situation.

The Wannier functions w_n are a set of orthogonal functions obtained from the Bloch functions $\phi_q^{(n)}$ [27]:

$$w_n(x - x_j) = \frac{1}{Z}\sum_q e^{iqx_j}\phi_q^{(n)}(x).$$

Above, Z is some normalization constant, and if L is the even number of sites in the lattice[1], $q = 2\pi j/L$ where j is an integer running from $-L/2$ to $L/2 - 1$.

Whereas a Bloch function is delocalized, a Wannier function becomes more and more peaked at the lattice site x_j as the lattice height is increased. Therefore, it can be useful to describe localized particles. This tendency toward localization is expected, since the deeper the lattice, the smaller the tunneling probability, and therefore the more localized near one given site atoms are.

Thus, the Wannier functions are useful to discuss phenomena in which a strong spacial localization in a periodic potential takes place. Note that we retain only the lowest in energy, w_0, and neglect excitations, that is, higher bands.

To derive a discrete form of the Bose-Hubbard Hamiltonian from the continuous model (2.1) (done in [23]), the bosonic field operator are written with the lowest Wannier function only:

$$\Psi(x) = \sum_j w_0(x - x_j)a_j,$$

where the x_j localize the minima of the optical potential, and a_j is an annihilation operator acting at x_j. Moreover, we keep only on-site interactions, because they are the most important, due to the strong localization (see appendix B of [28] for a detailed justification) we obtain:

$$H = -J\sum_i (a_i^\dagger a_{i+1} + a_{i+1}^\dagger a_i) + \frac{U}{2}\sum_i a_i^\dagger a_i^\dagger a_i a_i. \tag{2.2}$$

[1]Then, if a is the interspace between two sites (the lattice period), La is the total size of the lattice. However, to simplify, we take $a = 1$ in the following.

First presented in a seminal paper by M. P. A. Fisher in 1989 [15], this very simple expression –however physically rich– features a kinetic term (the first) in the form of a trend toward displacement from site j to site $j+1$. Here, another simplification is done by supposing that jumps of more than one site at once is impossible: terms like $a_i^\dagger a_{i+2}+$ h.c. are neglected. In more refined models, however, they could appear (see [25]), but would only marginally alter the physics. Thus, the parameter:

$$J = \int d^3x w_0(x - x_i) \left(-\frac{\hbar^2}{2m}\nabla^2 + V_{\text{external}}(x) \right) w_0(x - x_j), \tag{2.3}$$

can be viewed as a positive *hopping parameter*, measuring the probability of tunneling from one site to its closest neighbor.

The second term, which, from bosonic commutation relation, can be expressed as:

$$V_{\text{interaction}} = \frac{U}{2} \sum_i a_i^\dagger a_i (a_i^\dagger a_i - 1) = \frac{U}{2} \sum_i n_i(n_i - 1),$$

with the local density operator n_i, giving exactly the number of particles located at site i. This term vanishes at sites empty or occupied by only one particle. For higher occupation, it gives U times the number of possible pairs: 1 for $n_j = 2$, 6 for $n_j = 4$, etc. Thus it describes, in an intuitive manner, the interaction between particles. Its expression in term of the Wannier function and experimental parameters (mass and s-wave scattering length) is:

$$U = \frac{4\pi a_s}{m} \int d^3x |w(x)|^4.$$

Yet simple in its expression, the Bose-Hubbard model is in general not solvable exactly: for N atoms spreading over L sites, the dimension of the Hilbert space is:

$$D = \frac{(L + N - 1)!}{N!(L - 1)!},$$

if the total number of atoms is conserved[2], $D = N^L$ otherwise. For small lattice sizes, $L = 7 - 10$, exact diagonalization is possible with the Lanczos method [34], but as D grows exponentially, one is forced to use approximate, numerical methods. An efficient one, called the Density Matrix Renormalization Group, will be described in chapter 3.

These efforts are worth, because the competition between the interaction, which acts to localize particles, and the kinetic (hopping) term, which does the contrary, produces fascinating effects. In particular a rich phase diagram, exhibiting, in one dimension, a critical point at $U/J \approx 3.37$, when the filling L/N is equal to one [14]. Moreover, as Both J and U are tunable, this model is particularly suited for experimental studies (see for instance [19] and references therein), what is discussed in the following sections.

2.2 Quantum phase transition in the Bose-Hubbard Model

The Bose-Hubbard Hamiltonian can be solved exactly in two limiting cases: when hopping is completely neglected, and when interactions are. In this section, we begin by exploring

[2]Which will always be the case for us.

them, in order to have a clear idea of the physics at least for the extremes $U/J = 0$ and $J/U = 0$. Whereas at incommensurate fillings (N/L not an integer) the phase is the same for both limits (superfluid), it is not for $J = 0$ in a commensurate filling (N/L is an integer). The obtained state, so-called Mott-insulating, is gapped. Armed with this, we investigate, with the help of a numerical scheme described in the next chapter, the cases when U/J is finite and non-zero.

With an incommensurate filling, the same phase remains, whatever the ratio U/J. This is not the case with commensurate filling, where a phase transition is expected from Mott to Superfluid state. This is the interesting situation, on which we focus our attention. We present several ways to distinguish between the two phases: one-body correlation, fluctuation in the occupation number, momentum distribution. The aim is not to pinpoint the critical as was done in [14, 15], but to present an overview, and to focus on the tools which will be important in the next chapters, namely one-body correlations and momentum distribution.

2.2.1 The Mott Insulator and Superfluid Ground States

In the limit of strong interaction (that is, $J/U \to 0$), the Bose-Hubbard Hamiltonian reduces to:

$$H = \frac{U}{2} \sum n_i(n_i - 1),$$

which is diagonal in the Fock occupation basis; this basis is formed by Fock vectors $|n_1, n_2, ..., n_L\rangle$ where $n_i = 0, 1, ..., N$ provided $\sum_i n_i = N$. Imagine that the filling $\bar{n} = N/L = 1$. In this case the ground state is simply the state with one particle per site, because it costs a lot of energy to form a pair and leave a vacant site. Localization is therefore maximal. Moreover, the energy levels are clearly located at $0, U, 2U, ...$, because the spectrum of the operator $n_i(n_i - 1)/2$ is $\mathbb{N}$. Therefore, an energy gap exists in this limit.

This localization forbids any transport of particle in the ground state, and because of the gap, the system is an insulator, so-called Mott Insulator state. However, this state is easily destroyed: there suffices to add a particle on top of this state to suppress the gap. Indeed, in a simplified picture, the excess particle has no preferred location and moves freely on top of an array of particle. It is delocalized, and consequently the whole system is. As a consequence transport phenomena are now allowed and the state is no more an insulator state, but a superfluid state.

Thus, one sees that Mott insulator state only happens at *integer fillings*. In the first case above, we had $\bar{n} = 1$, but in the second, $\bar{n} = (L+1)/L = 1 + 1/L$, which can not be an integer. However, the Mott Insulator state can also be suppressed when U/J becomes too small, that is, when hopping starts to delocalize particles. For filling $\bar{n} = 1$, a phase transition to a superfluid state takes place, at $U/J \approx 3.37$ (in the thermodynamic limit, that is, $L \to \infty$, keeping $\bar{n}$ constant) [14, 31], rather smoothly. Closely around the critical value, the system is found in a intermediate Kosterlitz-Thouless phase [26].

Now, we switch to the opposite limit, of vanishing interaction, where the bosons are free: with the hopping term alone, they move freely on the lattice. The Hamiltonian reduces to:

$$H = -J \sum_i a_i^\dagger a_{i+1} + a_{i+1}^\dagger a_i,$$

and can be diagonalized by a Fourier transform. The creation operator becomes:

$$a_q^\dagger = \frac{1}{L}\sum_{l=0}^{L-1} e^{i\pi ql/L} a_l^\dagger,$$

and the Hamiltonian is transformed into:

$$H = -2J\sum_{q=0}^{L-1} \cos\left(\frac{q\pi}{L}\right) a_q^\dagger a_q. \tag{2.4}$$

The eigenstates of the Hamiltonian have eigenenergies $E_q = -2J\cos\left(\frac{q\pi}{L}\right)$, and the state of lowest energy ($q = 0$) can be written as:

$$|\psi_0\rangle = \frac{(a_{q=0}^\dagger)^N}{N!}|0\rangle,$$

where $|0\rangle$ is the vacuum.

This state is also a superfluid. So far, out of three cases, we found a Mott insulator in only one case. The table below summarizes the situation.

Filling	*U*	*J*	*State*
Incommensurable	Any	Any	Superfluid
Commensurable	Any	0	Mott Insulator
Commensurable	0	Any	Superfluid

Now, with this knowledge of the limiting cases, we go to a more general situation where U and J are both finite and non-zero, and study numerically several observables.

2.2.2 Energy in the Bose-Hubbard Model

The first observable to look at is of course the eigenenergy of the ground state. To do so, we choose to vary the ratio U/J. Thus, in figure 2.1 for example, localized systems (because the filling is one), with high interaction stength as compared to the hopping, lies at the right side. Towards $U/J = 0$ lies the superfluid, delocalized states. This is where the energy grows the fastest with U/J. By contrast, it tends to 0 as $U/J \to \infty$. The ground state itself tends to the maximally localized state, a so-called "atomic" state [15], $\otimes_{i=1..L}|1\rangle$, simply the tensor product state with eigenenergy 0.

However, energy tends to 0 only when $\bar{n} \leq 1$, when there are more sites than particles. If, in contrast, $\bar{n} > 1$, at least two particles are always interacting, and the energy has no upper bound. The band-structure of the Bose-Hubbard model is difficult to find. Without hopping, it is simple the countable set $\{0, U, 2U, ...\}$, for any momenta. But the kinetic part introduces a k-dependence and a certain bandwidth; see for example [43] for Monte-Carlo calculations.

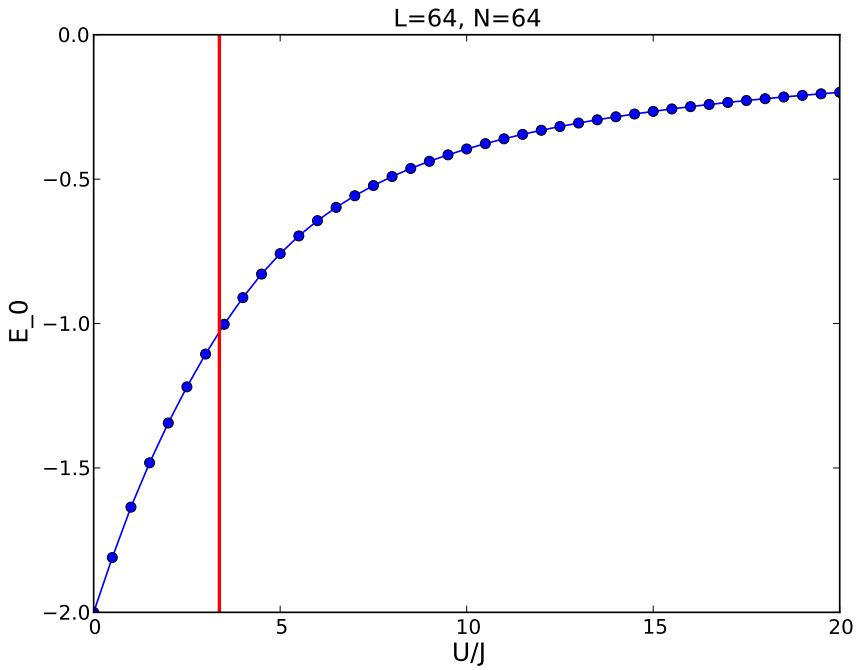

Figure 2.1: Groundstate energy of a system of 64 sites with unit filling, versus the ratio U/J. The vertical line at $U/J = 3.37$ locates approximatively the transition point, according to [31]. The energy at $U/J = 0$ is exactly $E_{q=0} = -2.0$. When $U/J \to \infty$, every particle have one and only one site to populate, and therefore, the ground state is a simple atomic Mott state with 0 energy.

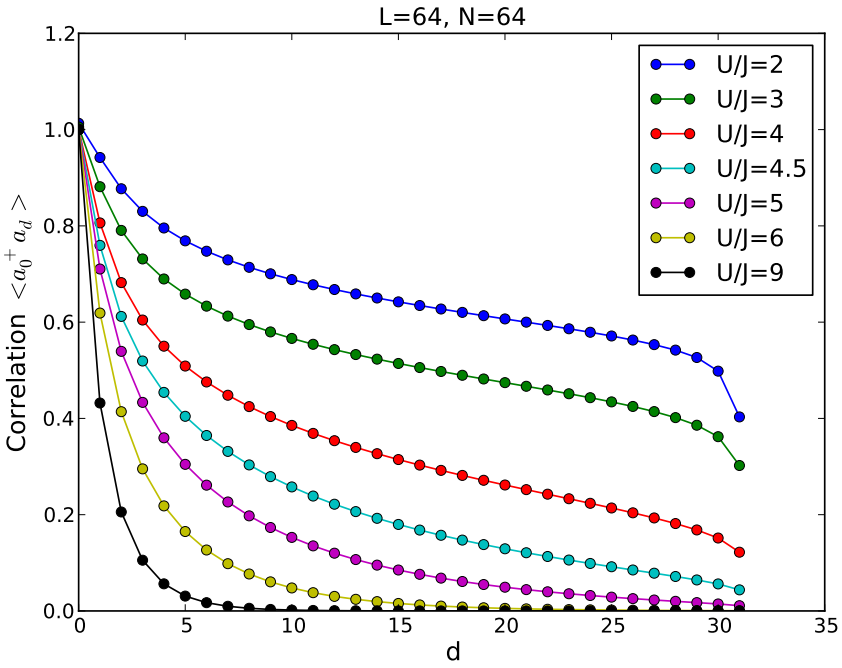

(a)

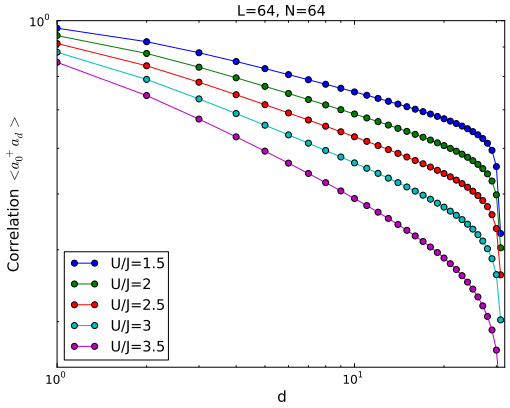

(b) Log-Log scale

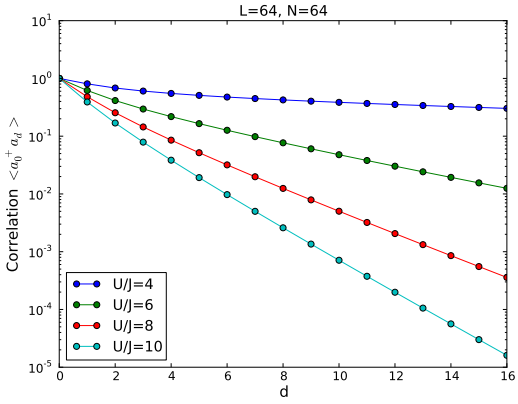

(c) Semi-logarithmique scale

Figure 2.2: One-body correlation function $\langle a_0^\dagger a_d \rangle$, versus the distance d, for various ratios U/J, at a commensurate filling, $\bar{n} = 1$. In (a), one sees how fast the correlations drop to 0 for $U/J > 3.37$, so in the Mott insulator state. Those states are weakly correlated, the decrease is exponential, as (c) shows. By contrast, in (b), the ground state is superfluid, and one-body correlations decrease slowly, following an algebraic law. A connection persists even for sites far apart: in a superfluid, particles are coherent. Note a little drop at $d \approx L/2$: this is a slight boundary effect. Note that, though our system is large enough to see the exponential and algebraic decays, it would not be correct to determine a correlation length from these data. Its value would suffer from finite-size effects.

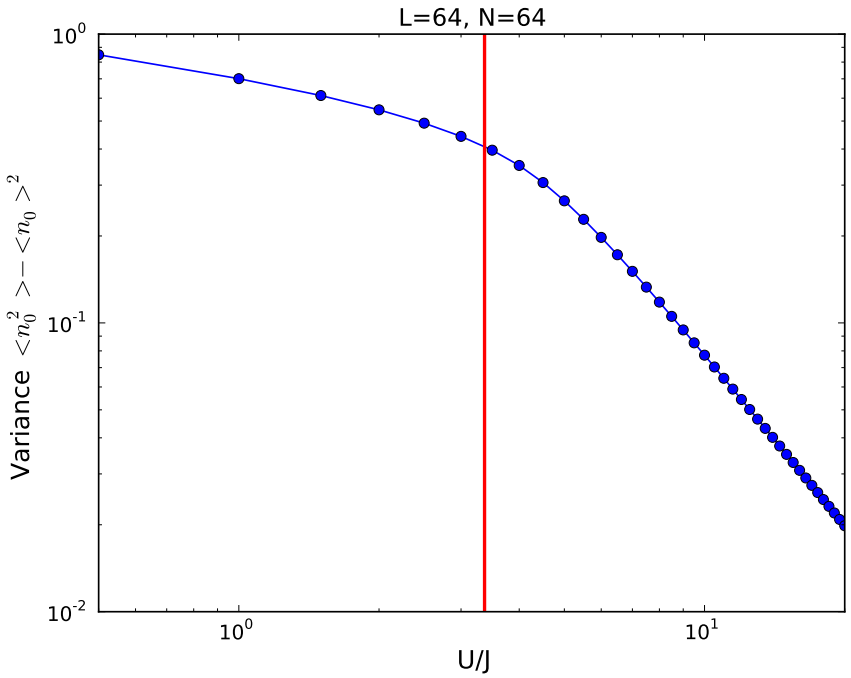

Figure 2.3: Variance of the occupation number, $\langle n_0^2 \rangle - \langle n_0 \rangle^2$. The red line at $U/J = 3.37$ indicates approximatively the critical point. The algebraic decaying (linear decaying in a log-log scale) in the Mott insulator state is clear, but the regime is different in Superfluid. Moreover, the linear regime ceases slightly after the red line, indicating a intermediate phase (Kosterlitz-Thouless).

2.2.3 One-body Correlation Function and Occupation Variance

In this section, we consider the one-body correlation functions, $\langle a_0^\dagger a_d \rangle$. a is the annihilation operator, 0 denotes the center of the lattice and d some distance with respect to this middle. The bracket $\langle\rangle$ is a quantum mechanical average over some central sites, so as to cancel possible boundary effects.

As figure 2.2 (a) shows, for small U/J, the freedom of the atoms on the lattice results in strong one-body correlations between them (blue, green and red lines). However, in one-dimension, no true long-range order exists, i.e. $\langle a_0^\dagger a_d \rangle$ approaches 0 for $d \to \infty$: in the superfluid phase, $\langle a_0^\dagger a_d \rangle$ decays algebraically [17],

$$\langle a_0^\dagger a_d \rangle_{\mathrm{SF}} \propto d^{-K/2},$$

where K is the Luttinger parameter. This decay can be seen in 2.2 (b): in a log-log scale, $\langle a_0^\dagger a_d \rangle$ decays almost linearly. However, notable boundary effects bend the curve more and more as d increases. These effects, as well as finite size effects (due to the small value of L), modify the value of K, which universal value can not be determined safely with such a small system.

This algebraic decay is a peculiarity of one-dimensional systems, which does not exist in higher dimensions. In one-dimension, the high quantum fluctuations are responsible for this algebraic decay (see below).

In contrast, as U/J grows, particle number fluctuations become energetically costly and correlations are rapidly suppressed (see purple, yellow and black lines of 2.2 (a)). Their decay is exponential in the Mott-insulating state [17]:

$$\langle a_0^\dagger a_d \rangle_{\mathrm{MI}} \propto \exp(-d/\xi).$$

Here ξ is the correlation length. Figure 2.2 (c) shows this exponential decay in a semi-logarithmique scale. In this state, particle number is well determined on each site and the system shows no phase coherence.

The importance of quantum fluctuations in the superfluid phase can also be caught by the variance of the occupation number n_0 of the central site,

$$\sigma_0^2 = \langle (n_0 - \bar{n})^2 \rangle.$$

This quantity measures the statistical fluctuations in the occupation of the middle site. It is shown in Figure 2.3. They are high in the superfluid regime, because a the number of atoms located at the same site can fluctuate due to delocalization. But, as already noted in figure 2.3, they are clearly suppressed in the Mott Insulator region. As correlations do, the occupation fluctuations decay algebraically.

2.3 The Momentum Distribution

In this section, we introduce an important quantity, the momentum distribution, which can be though as a Fourier transform of the one-particle correlation function. We first show that this is one of the easiest measurable quantity by so-called time-of-flight measurements, easier to obtain than, for example, the density n_i. Then, we explain why it provides in fact more informations on the system than the sole density n_i. Finally, we calculate numerically the momentum distribution in several cases to see more precisely how to discriminate between superfluid and Mott-insulating states.

2.3.1 Introduction and Experimental Considerations

The density distribution $n(x, y, z)$ of a three-dimensional atom cloud can be measured by absorption imaging. In this technique, the cloud is illuminated by a laser beam. The atoms absorb light and therefore attenuate the beam; if the laser propagates in the z direction with intensity $I_0(x, y)$ before its passage through the cloud, it reads, after the passage [19],

$$I(x, y) = I_0(x, y)e^{-D(x,y)},$$

where the optical density $D(x, y)$ is proportional to the integrated density $n(x, y, z)$ along the propagating axis z,

$$D(x, y) = \frac{\alpha\lambda^2}{2\pi} \int_z n(x, y, z)dz.$$

α is a factor which depends only on the laser beam, not on the cloud state. $\lambda/2$ is the lattice spacing. Thus, by measuring the ratio I/I_0, the integrated column density can be obtained directly. However, this presents two drawbacks.

First, this technique is destructive, because the photons brought by the laser scatter incoherently with the cloud and heat it strongly, resulting in the loss of the sample. Moreover, the laser has to pass throughout a cloud of very high optical density, which is in general not possible, because the density is too high.

This density has to be lowered by letting the cloud expand freely and ballisticaly for a while. This is possible because, even before any optical potential, some confining potential has to be introduced, simply to gather all the atoms and isolate them from the external environment [19]. This is done by a magnetic trapping potential of harmonic shape. The atoms naturally populate the bottom of this trap, where lies its minimum.

Therefore, before imaging, all trapping potential are turned off and the cloud expands. It is only after a certain time, so-called time-of-flight, usually between 2 and 20 ms [19], that the imaging process in launched. Therefore, it is not exactly the spatial density n which can be measured, but the momentum distribution, because the cloud expands according to the momentum distribution of the atomic cloud.

Secondly, the optical resolution of the imaging systems is larger than the lattice spacing. In [19], where atoms of ^{87}Rb were used, the lattice spacing was as small as $\lambda/2 = 425$ nm. It was not possible to resolve individual sites and therefore n_i remained unknown (nowadays, however, this becomes possible). But this is not a problem, because the momentum distribution carries actually more information about the cloud, and can be accurately obtained in time-of-flight measurements.

In such measurement, once the atomic cloud is believed to be in the desired state, the trapping potentials are switched off. Consequently, particles can move across the lattice. As we mentioned, they are well described by the Wannier functions. These wavepackets spread and overlap with each other, while the cloud expands. This produces interferences which can be imaged. The quantity recorded is the momentum distribution, which, provided interactions during the flight can be neglected [19], is the Fourier transform of the original macroscopic wave function in the lattice.

If the optical lattice height was high, the atoms experienced a strong lattice potential and were confined. Their wavefunction can be approximated by a Gaussian with a certain width, which depends on the exact value of U. Its Fourier transform is then also a simple Gaussian, and the momentum distribution will be an isotropic Gaussian. The width of

the Gaussian is the inverse of the ground state expansion around a site, once its increase due to the expansion of the cloud during the flight is substracted. Macroscopically, in the Mott-insulating state, there is comb-like wacefunction, very localized peaks without overlaps.

In contrast, with a shallow lattice potential, the local wavefunctions can not be approximated by Gaussian. Delocalized over the lattice, the wavefunctions overlap, and a large phase coherence exists. The Fourier transform will show peaks arrayed in the reciprocal lattice of the lattice created the laser beams (optical lattice). The width of these peaks is the inverse of the extension of the wavefunctions at each site (coherence length). Macroscopically, this means a smooth, global wave-function non-zero everywhere.

This fact was observed experimentally in section 4.2 (figure 4.11) of [19]: a 2D superfluid cloud (shallow lattice) yielded an interference pattern with narrow peaks in it, arranged in simple (square) periodic structures, after a time-of-flight of typically 15 ms. On the contrary, with a deep Mott insulator (so a high lattice depth), the interference pattern is completely absent, replaced by an isotropic Gaussian.

Therefore, besides the density distribution n_i which provides direct information on the system, the momentum distribution is also interesting, because it gives indications about the many-body state of the atoms before their release from the trapping potentials, and allows to distinguish with a good precision between superfluid and Mott insulating states, from the difference of coherence in the two states.

2.3.2 Momentum Distribution from DMRG Calculations

In this section we calculate numerically the momentum distribution and examine if the statements of the previous section are verified.

In general, the momentum distribution is given by:

$$n_k = \frac{1}{L}|w(k)|^2 \sum_d e^{ikd}\langle a_0^\dagger a_d\rangle, \tag{2.5}$$

where $w(k)$ is the Fourier transform of the associated Wannier function. Because the Wannier function in real space is localized, the factor $|w(k)|^2$ is a slowly varying envelope which will be neglected in the following. DMRG gives access to $\langle a_0^\dagger a_d\rangle$, and therefore to the momentum distribution. Exact calculation with a $L = 10, N = 10$ system were done in [44], and an hydrodynamical approach in [37]. In [28], the influence of the parabolic trap were investigated, and the decay of the peak height and the width is studied to discriminate between superfluid and Mott-insulator phases with a good precision.

Figure 2.4 shows $n_k - \bar{n}$ (we substract $\bar{n}$ because it is the constant contribution for $d = 0$). As expected from the previous section, a peak is seen in the superfluid phase (curves with circle markers) at $k = 0$, with a 2π-periodicity. However, there are additional smaller peaks arising from finite-size effects [28]. In the Mott-insulating state (curves with square markers), for U/J high enough, the peaks have completely disappeared, no phase coherence remains in the system. At $U/J = 7$, the momentum distribution is yet not completely flat, indicating residual coherence, which disappears as U/J is further increased.

This is in good agreement with the statements of the previous section; the only added feature is the finite-size effects, which introduce additional minor interference peaks in

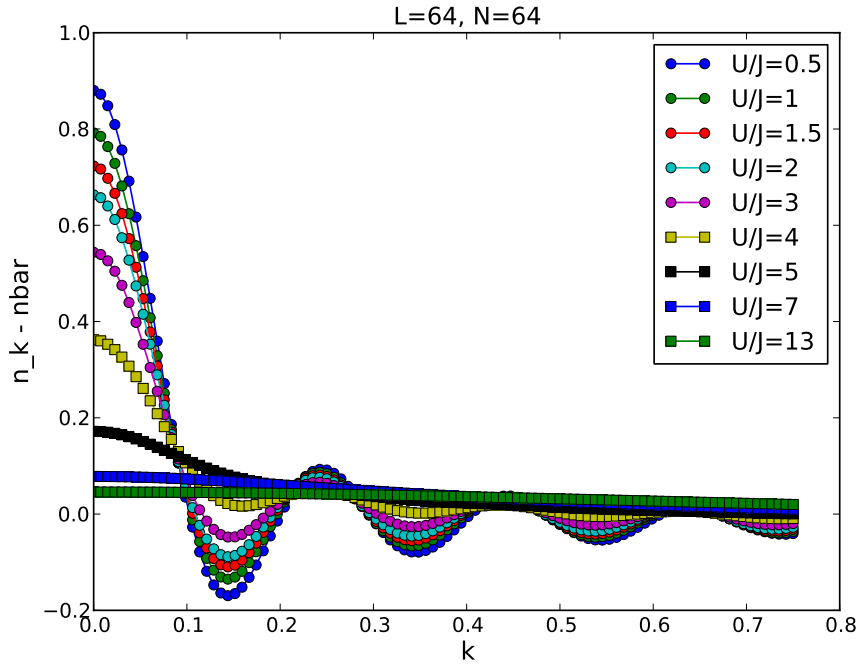

Figure 2.4: Momentum distribution $n_k - \bar{n}$ for several values of the interaction strength U, where $\bar{n} = 1$ is the filling factor. Negative values are due to the substraction. A peak at $k = 0$ is seen is the superfluid phase (curves with circle markers), along with additional peaks due to finite-size effects. In the Mott state (curves with square markers), the distribution is very flat, and only a residual coherence persists.

the superfluid phase. In the following chapters, we will use extensively the momentum distribution to explore non-equilibrium properties of a system. Before this, we introduce the dynamic of a quench with an example from the literature.

2.4 Dynamics with the Bose-Hubbard Model

2.4.1 Motivation

In the previous sections, we used one-body correlations to characterize the low energy properties of quantum many-body states. We saw how they can be used to discriminate between superfluid and Mott-insulating phases, either directly or after a transformation, via the momentum distribution. However, dynamics also raises interest: How does a system evolve far from equilibrium ? We also insisted on the fact that the parameters in the Bose-Hubbard Hamiltonian, the interaction strength U and the hopping parameter J, are highly tunable. In particular, it is nowadays possible [19] to change suddenly the value of some parameter. Thus, some ground state can be suddenly brought into a new set of parameters for which this state is not the ground state anymore. It undergoes a non-equilibrium dynamics, and thus, non-equilibrium quantum many-body states can be easily created and studied by the setup introduced in 2.3.1.

Fundamental questions raised are, for example, How does the state evolve ? Starting from a superfluid ground state, if the lattice height is suddenly increased, the state intuitively, should move toward the ground state of the final Hamiltonian. However, because of energy conservation, revival of the initial state will occur. As time goes on, the intuition is less clear, and the system will be found in an intriguing non-equilibrium state. What is the period of this revival ? In this section, we show, that, for a quench in the interaction parameter, within some approximation it is $\nu_0 = 2\pi/U_{\text{final}}$, where U_{final} is the final interaction (after the quench).

However, the situation is not so simple, and after a few revival the simple picture developed fails. The reason is, the evolution operator, $e^{-iH_{\text{final}}t}$ can only be diagonalized in its interaction part. Hopping presents difficulties, and is responsible for the loss of periodicity. Observables evolve in a messy pattern after about $3\nu_0$.

Another general question is, How fast can information propagate ? One-body correlations $\langle a_0^\dagger a_d \rangle$ links distant sites; distant particles will feel the quench after longer times than nearest-neighbors. This gives a notion of a propagating signal. Is there a speed limit on this propagation ? Lieb and Robinson found indeed an upper bound on the spreading velocity of correlation [35], in the case of spin systems. For the Bose-Hubbard model, several studies were already led [36, 9], and also found a finite velocity. In this section, we briefly present the results of [36] so as to get a feeling with the general dynamics.

2.4.2 Quenches from the Superfluid Ground State

We consider a 1D system in its superfluid ground state, $U/J < 3.3$. If we suddenly increase the interaction strength to large values, we expect the one-body correlations (or density correlations) to lower toward Mott-insulating values – however not the ground state values, because energy, in our case, is conserved, and a Mott-insulator ground state has larger energy than a superfluid one. But this shift is far from trivial and some memory

of the initial one-body correlations may persist, even after long times. In the meantime, transient phenomena, such as oscillations, short revivals of the initial state [19], may take place, depending on the range $U_{\text{initial}} - U_{\text{final}}$.

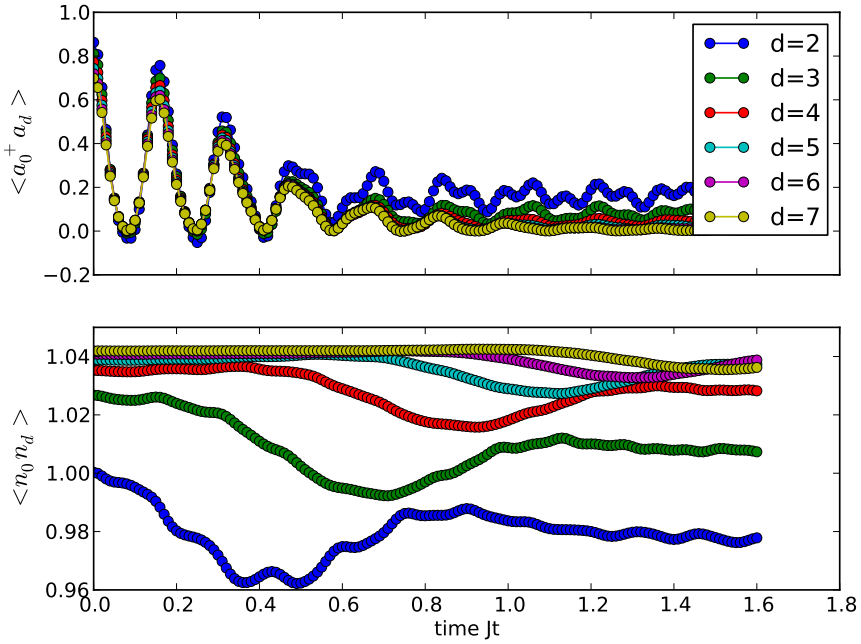

Figure 2.5: Time evolution of one-body (top) and density correlations (bottom) for the quench described in the text, $U = 2 \to 40$, for different distances d. On top, $\langle a_0^\dagger a_2 \rangle$ for example shows a revival after $2\pi/U$ and $4\pi/U$. The amplitudes are clearly attenuated [29]. But further, a quasi-steady-state is reached, in which correlations present small oscillations in a messy pattern. By looking at the time at which this regime is reached for each d, a propagation velocity can be extracted, as was done in [36]. Similarly, on bottom panel, $\langle n_0 n_2 \rangle$ presents a minimum at $Jt \approx 0.45$, which moves approximately linearly with d. The location of this minimum can also be used to determine the propagation velocity.

In general, the time evolution of the ground state with respect to H_{final} is governed by the Schrödinger equation,

$$|\Psi(t)\rangle = \exp(-iH_{\text{final}}t)|\Psi(0)\rangle.$$

We can expand $|\Psi(0)\rangle$ in the Fock basis:

$$|\Psi(0)\rangle = \sum_n c_n |n\rangle,$$

where $|n\rangle$ denotes some occupation configuration of $\bar{n}L$ particles on the lattice. If we neglect the hopping part of the Bose-Hubbard Hamiltonian, keeping only the local interacting part, those Fock states become eigenstates of the Hamiltonian. The expectation value of some operator O can then be written:

$$\langle \Psi(t)|O|\Psi(t)\rangle = \sum_{n,n'} c_n^* c_{n'} \exp(-i(E_n - E_{n'})t)\langle n|O|n'\rangle, \tag{2.6}$$

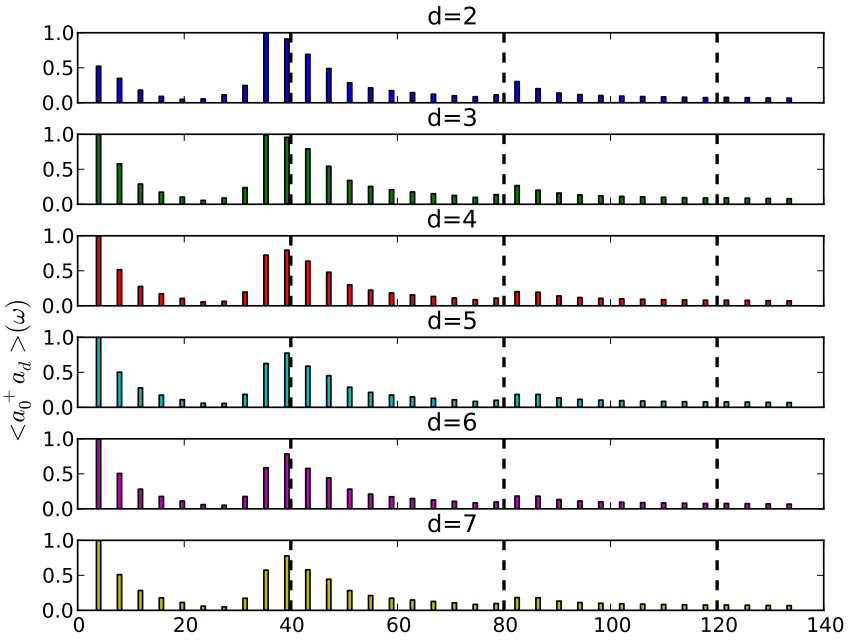

Figure 2.6: Fourier transform of the correlations $\langle a_0^\dagger a_d \rangle$ versus frequency ω (in units of J), for several distances d. For clarity the peak at $k = 0$ is omitted. The vertical dashed lines are at $\omega = nU$ for $n = 1, 2, 3$. Peaks can be seen, at least for $n = 0, 1, 2$, with a large bandwidth at $n = 2$. This bandwidth is the due to the hopping J and cannot be understood in the simple approach developed in the text.

where E_n is the interaction energy of state $|n\rangle = |n_1, n_2, ..., n_L\rangle$,

$$E_n = \frac{U_{\text{final}}}{2} \sum_{i=1}^{L} n_i(n_i - 1).$$

Thus, in the limit of strong interactions, the evolution of correlation functions can be estimated. Writing $a_i^\dagger$ for the creation operator at the site i and a_j for the annihilation operator at site j, we have (supposing $1 < i < j < L$):

$$\begin{aligned}\langle n_1, ..., n_L | a_i^\dagger a_j | n'_1, ..., n'_L \rangle &= \langle n_1, ..., n_L | n'_1, ..., n'_i + 1, ..., n'_j - 1, ..., n_L \rangle \\ &= \sqrt{n'_i}\sqrt{n'_j + 1}\delta_{n_1,n'_1} ... \delta_{n_i,n'_i+1} ... \delta_{n_j,n'_j-1} ...\end{aligned}$$

Thus,

$$\langle a_i^\dagger a_j \rangle = \sum_{n,n'} \delta_{n_i,n'_i+1}\delta_{n_j,n'_j-1} c_n^* c_{n'} \exp(-iU_{\text{final}}(n'_j - n'_i - 1)t)\sqrt{n'_i}\sqrt{n'_j + 1}.$$

This is a sum of oscillating terms at frequencies $\nu = 2\pi n/U_f$, where $n = n_k - n_j - 1$ is an integer. Figure 2.5 shows those correlations. Such oscillations can be seen during two periods (for $d = 2$), before a new regime is reached, in which the above picture is not true anymore. The effects of the hopping cannot be neglected anymore.

The superposition of frequencies can be made explicit by the Fourier transform, which will show peaks at multiples of U_f. In figure 2.6, we can see peaks near $n = 0, 1, 2$. This means:

$$n_k - n_j = 1, 2 \text{ or } 3,$$

with a clear preference for 1,2, except maybe at small d. Thus, the occupation fluctuates up to three particles for all distances; higher fluctuations are much rarer.

Coming back to the real data, we can see clear oscillations persisting, for $d = 2$ for instance, for almost 3 periods, when the effect of the hopping starts to be important. Before, the interacting part dominates and induces regular oscillations. Physically, the system, at times $2\pi n/U_f$, becomes much less correlated than its final averaged values, which is quite fascinating. One-body correlations, as well as density correlations, quickly lower to Mott-insulating value, but then, in half-period, reach their initial superfluid values. The non-hopping picture predicts this alternating scheme forever; but J can not be cast to 0. The kinetic part of the Hamiltonian drives the systems toward a quasi-steady state, with instabilities, small variations, whose behavior remains unclear.

In [29], a simple model in terms of Bessel's function is developed, so as to take into account this finite bandwidth ($\approx 6J$) of the Bose-Hubbard model. They manage to reproduce the decrease of the peaks towards a steady value.

How could we extract some kind of sound velocity from these data ? One can decide when $\langle a_0^\dagger a_r \rangle$ becomes messy, that is, when the large, regular oscillations ceased for a meandering curve. However, if we come back to (2.6), we can see that the density-density correlations should read:

$$\langle n_i n_j \rangle = \sum_m |c_m|^2 \langle m | n_i n_j | m \rangle ,$$

and should therefore remain constant, because $n_i n_j$ is a diagonal operator in the Fock occupation basis. It does not, however, once more because of the final value of J. Looking at figure 2.5, we see $\langle n_0 n_6 \rangle$ remaining constant until $t \approx 0.9J$, where it begins to drop. After reaching a minimum at $t \approx 1.3J$, it rises again to a plateau. This behavior can be linked with the arrival at site $L/2 + 6$ of some quasiparticle excitation, produced at site $L/2$ and at time $t = 0$, induced by the quench. This excitation seems to be endowed with some width, like a Gaussian wave propagating. The position of the minimum of $\langle n_0 n_r \rangle$ can thus be used to extrapolate a velocity from the formula $v = r/t + v_0$, with some constant v_0.

The relation between r and t is found linear in [36] for a wide range of initial and final interaction, and also different fillings $\bar{n}$. Several approximation methods (continuous Lieb-Liniger model, bozonisation, etc.) are also presented in order to predict the values of this velocity.

In this section, we showed that, after a quench, correlations "spread" with a certain velocity. They show a few oscillations with period $2\pi/U_{\text{final}}$, but, because of the finite tunneling probability, a messy pattern rapidly supersedes the simple prediction obtained with a purely interaction Hamiltonian. However, the latter allows to understand partly the situation, and why there are two different regimes of oscillation. In the next chapters, we will focus on a different situation, with initial U/J deep in the Mott-insulating region. In such region, the hopping part of the Hamiltonian may be treated perturbatively. Though the configuration is opposite, the same tool will be available to extract a propagation velocity.

Chapter 3

Methods

This chapter is devoted to the methods which will serve the analysis of a non-equilibrium quantum many-body states in chapter 4. The Density Matrix Renormalization Group (DMRG), presented in section 3.1, were already used in the previous chapter. It is a variational scheme particularly suited for physical problems on a lattice, either finite of infinite. We present the idea and pay a particular attention to its limitations and its control parameters. DMRG for ground state calculations as well as time-evolution are considered.

In the second part, 3.2, we develop a perturbative analysis of the time-evolution of an atomic Mott state. Because it can be written as a simple tensor product, this eigenstate of the Bose-Hubbard Hamiltonian with $J = 0$ is suited for this kind of treatment. The hopping in introduced as a perturbation. We show that this analysis is very good for quenches down to $U/J \approx 20$, and over large timescales by examining an observable, $\langle a_0^\dagger a_d \rangle$ and comparing them to DMRG data. In conclusion, we give clue toward other approximative methods potentially better than simple quantum perturbation theory.

3.1 The Density Matrix Renormalization Group Method

Density Matrix Renormalization Group (DMRG) [45] was invented in 1992 by S. White [52] and proved to be one of the best algorithm to study one-dimensional systems on a lattice [46], along with quantum Monte-Carlo, exact diagonalization, series expansion and coupled cluster expansion. Time-evolution [7, 51], low-lying properties of virtually any one-dimensional systems can be unveiled by DMRG, including infinite-size systems, and since recently, dynamical quantities such as the dynamical correlation functions [30] are also accessible. Moreover, extensions of DMRG were developed to treat systems at finite-temperature [47].

In section 3.1.1, we present the idea at the foundation of DMRG, the Matrix Product State, which consist in a clever writing of a quantum state. Instead of specifying a explosively large set of probability amplitude, a set of matrix can be used. By setting an upper limit on their size, the amount of number required can be made manageable with controllable loss of precision (section 3.1.2). Expectation values of operator can be calculated easily (section 3.1.3). Then the ground state is obtained variationally (section 3.1.4), and the time-evolution of any MPS obtained by a Trotter-Suzuki decomposition of the evolution operator e^{-iHt} (section 3.1.5).

3.1.1 Matrix Product States

Start with a one-dimensional lattice of L sites, with a local state space $\{\sigma_i\}$ on each site $i = 1, ..., L$. For spin 1/2 for example, we would have $\sigma_i = \{+1/2, -1/2\}$, for bosons, $\sigma_i = \{0, 1, ..., N\}$ where N is the maximum number of particle at site i. The most general pure quantum state reads:

$$|\Psi\rangle = \sum_{\sigma_1,...,\sigma_L} c_{\sigma_1,...,\sigma_L} |\sigma_1, ..., \sigma_L\rangle.$$

We have to deal with a large number of coefficients $c_{\sigma_1,...,\sigma_L}$, which explodes with L (or N if we have bosons). The first step is to find a new way to write down a quantum state, not as a row of coefficients, but as a Matrix Product State. Although at first glance it will seem that the number of coefficients is even higher, with a clever truncation this number will become manageable.

Let us assume that the local dimension of the Hilbert space is d. Then the full Hilbert space has dimension d^L, which is also the number of coefficients $c_{\sigma_1,...,\sigma_L}$. The first step is to reshape this set into a matrix Ψ of dimension $d \times d^{L-1}$:

$$\Psi_{\sigma_1,(\sigma_2,...,\sigma_L)} = c_{\sigma_1,...,\sigma_L}.$$

The next step consists in decomposing the matrix Ψ into a product of three matrices by the Singular Value Decomposition (SVD) [49], so as to get:

$$\Psi_{\sigma_1,(\sigma_2,...,\sigma_L)} = \sum_{a_1} U_{\sigma_1,a_1} S_{a_1,a_1} V^\dagger_{a_1,(\sigma_2,...,\sigma_L)},$$

and to reshape back into a vector the product $SV^\dagger$. After those operations,

$$c_{\sigma_1,...,\sigma_L} = \sum_{a_1}^{r_1} U_{\sigma_1,a_1} c_{a_1,\sigma_2,...,\sigma_L} = \sum_{a_1}^{r_1} A^{\sigma_1}_{a_1} c_{a_1,\sigma_2,...,\sigma_L}.$$

For convenience we rewrite the matrix U as A, placing upper the physical indices σ_1 and lower the unphysical indices a_1, over which the sum is performed. The SVD decomposition is useful because U (or A) is left-normalized, $A^\dagger A = \mathbf{1}$. Moreover, S is diagonal, something which we will benefit from soon.

The idea now in to continue with $c_{a_1,\sigma_2,...,\sigma_L}$: reshape it, decompose it to get a set of d matrices A^{σ_2}, each of dimension $r_1 \times r_2$, and carry on. If we sweep throughout the lattice, we obtain:

$$c_{\sigma_1,...,\sigma_L} = \sum_{a_1,...,a_{L-1}} A^{\sigma_1}_{a_1} A^{\sigma_2}_{a_1,a_2} ... A^{\sigma_{L-1}}_{a_{L-2},a_{L-1}} A^{\sigma_L}_{a_{L-1}},$$

or, with implicit matrix multiplication:

$$c_{\sigma_1,...,\sigma_L} = A^{\sigma_1} A^{\sigma_2} ... A^{\sigma_{L-1}} A^{\sigma_L}.$$

So far all this looks very tedious and complicated, but the point will appear a bit later. At the moment, we have a new notation for the quantum state as:

$$|\Psi\rangle = \sum_{\sigma_1,...,\sigma_L} A^{\sigma_1} A^{\sigma_2} ... A^{\sigma_{L-1}} A^{\sigma_L} |\sigma_1, \sigma_2, ..., \sigma_{L-1}, \sigma_L\rangle,$$

so-called left-canonical Matrix Product State (MPS). In fact, changing a little the operations the physical sense underlying MPS can be made explicit. After l operations, we have:

$$c_{\sigma_1,...,\sigma_L} = (A^{\sigma_1}...A^{\sigma_l})_{a_l} S_{a_l,a_l} V^{\dagger}_{a_l,(\sigma_{l+1},...,\sigma_L)}.$$

We can decide to reshape $V^{\dagger}$ differently, as $\Psi_{(a_l,\sigma_{l+1},...,\sigma_{L-1}),\sigma_L}$ – instead of $\Psi_{a_l,(\sigma_{l+1},...,\sigma_L)}$ –, perform a SVD an go on this way until the end of the lattice. What we will obtain is:

$$V^{\dagger}_{a_l,(\sigma_{l+1},...,\sigma_L)} = \sum_{a_{l+1},...,a_{L-1}} B^{\sigma_{l+1}}_{a_l,a_{l+1}}...B^{\sigma_L}_{a_{L-1}},$$

where the matrices B are now *right* normalized, $BB^{\dagger} = 1$. In total, the coefficients c read:

$$c_{\sigma_1,...,\sigma_L} = A^{\sigma_1}...A^{\sigma_l} S B^{\sigma_{l+1}}...B^{\sigma_L},$$

with a diagonal matrix S. In the MPS language, this is called the mixed-canonical representation. If we write $S_{a,a} = s_a$, and introduce:

$$|a_l\rangle_A = \sum_{\sigma_1,...\sigma_l} (A^{\sigma_1}...A^{\sigma_l})_{a_l} |\sigma_1, ..., \sigma_l\rangle,$$
$$|a_l\rangle_B = \sum_{\sigma_{l+1},...\sigma_L} (B^{\sigma_{l+1}}...B^{\sigma_L})_{a_l} |\sigma_{l+1}, ..., \sigma_L\rangle,$$

the quantum state now reads:

$$|\Psi\rangle = \sum_{a_l}^{r_l} s_a |a_l\rangle_A |a_l\rangle_B,$$

which is exactly the Schmidt decomposition of a pure quantum state [41]. In this decomposition, the lattice is split in two parts, A and B. When s_a is just one number, this is only a product state. On the contrary, when the sum runs over several values, $|\Psi\rangle$ is an entangled state. In the latter, such a decomposition allows to read off easily the reduced density operators for A and B and therefore to calculate easily interesting quantities such as the von Neumann entropy [46]. This is a first advantage of the MPS over the classical representation of the state with an array of coefficients $c_{\sigma_1,...,\sigma_L}$.

3.1.2 Truncation of the MPS

Though we have a clever new notation for the quantum state, it is still impossible for any computer to handle exactly a MPS, except maybe for very small systems. The problem is that the size of matrices grows at each step: in a right canonical decomposition (with matrix A only), $1 \times d$ for the first site, $d \times d^2$ for the second, etc., until the central site, where the dimension is maximal, $d^{L/2-1} \times d^{L/2}$ (if L is even). The next matrix has dimension $d^{L/2} \times d^{L/2-1}$, and the dimensions decrease to $d^2 \times d$ and $d \times 1$ for the two last sites.

However, this difficulty is overcame by using the SVD. A maximal size D is sat on the matrix, and upon SVD a truncation is made to conserve only D rows and/or columns. How do we decide which one should be cut ? Since the matrix S is diagonal, it provides a "weight", in the form of a singular value, for each row/column, and there suffices to cut the ones corresponging the lowest singular values.

In other words, in a mixed-canonical representation, we write:

$$|\Psi\rangle = \sum_{a_l}^{r'_l} s_a |a_l\rangle_A |a_l\rangle_B,$$

with $r'_l < r_l$. This results in a loss of precision, but the Hilbert space is still complete. In general this truncation is possible because the singular values s_a decay exponentially [46]. It is possible to show [50] that the overall error is at worst:

$$||\Psi\rangle - |\Psi\rangle_{\text{truncated}}|^2 \leq 2 \sum_{i=1}^{L} \epsilon_i(D),$$

where $\epsilon_i(D)$ is the sum of the squared discarded singular values. In one-dimension, this error is manageable, but not in higher dimension [46].

3.1.3 Overlaps and Expectation Values

Before we turn to the ground state calculations, we need to be able to perform operations with MPS. Having two states $|\Psi\rangle$ and $|\Phi\rangle$, written as two MPS with matrices M and N (without necessary assumption on the normalization), their overlap reads:

$$\begin{aligned}
\langle\Psi|\Phi\rangle &= \sum_{\{\sigma\}} M^{\sigma_1 *} ... M^{\sigma_L *} N^{\sigma_1} ... N^{\sigma_L} \\
&= \sum_{\{\sigma\}} M^{\sigma_L \dagger} ... M^{\sigma_1 \dagger} N^{\sigma_1} ... N^{\sigma_L} \\
&= \sum_{\sigma_L} M^{\sigma_L \dagger} \left(... \left(\sum_{\sigma_1} M^{\sigma_1 \dagger} N^{\sigma_1} \right) ... \right) N^{\sigma_L}.
\end{aligned}$$

Written in the last form, the scalar product is incredibly simple to evaluate. If $|\Phi\rangle = |\Psi\rangle$ and the matrices are normalized, we immediately found that $\langle\Psi|\Psi\rangle = 1$. In this way, the number of operations done scales as $\mathcal{O}(LD^3d)$, which is reasonable, especially when compared to exponentially increasing number of operation we would have to do with the classical representation in term of a row of coefficients c.

Similarly, to evaluate expectation values such as $\langle\Psi|O|\Psi\rangle$, the operator O is written as:

$$O^l = \sum_{\sigma_l, \sigma'_l} O^{\sigma_l, \sigma'_l} |\sigma_l\rangle\langle\sigma'_l|,$$

on each site l. Then, obviously,

$$\begin{aligned}
\langle\Psi|O|\Psi\rangle &= \sum_{\{\sigma\},\{\sigma\}'} M^{\sigma_1 *} ... M^{\sigma_L *} O^{\sigma_1, \sigma'_1} ... O^{\sigma_L, \sigma'_L} M^{\sigma'_1} ... M^{\sigma'_L} \\
&= \sum_{\sigma_L, \sigma'_L} O^{\sigma_L, \sigma'_L} M^{\sigma_L \dagger} \left(... \left(\sum_{\sigma_1, \sigma'_1} O^{\sigma_1, \sigma'_1} M^{\sigma_1 \dagger} M^{\sigma'_1} \right) ... \right) M^{\sigma'_L}.
\end{aligned}$$

As before, the numerical cost of this operation is essentially $\mathcal{O}(LD^3d)$.

Thus, though is may be difficult to catch the interest of the MPS representation at the beginning, it quickly proves to be extremely efficient, at least in one-dimension, and able

to deal with potentially large lattice sizes L. It relies on the singular value decomposition to truncate the matrices, and the information lost can be minimized. The first advantage of MPS shows in the calculation of overlaps and expectation values which are extremely easy. In the next section, we explain why it allows to calculate the ground state also efficiently.

3.1.4 Ground State Calculation

At this point, we are virtually done. We know how to generate a vector $|\Psi\rangle$ randomly, simply by filling randomly all the matrices which dimensions are known, before normalizing them correctly. The size of these matrices is manageable, thanks to a particular truncation, which preserves the full Hilbert space. We are able to evaluate expectation values with this MPS, in particular the energy, $E|\Psi\rangle = \langle\Psi|H|\Psi\rangle$, where H is the Hamiltonian written in a matrix form similar to MPS. In this form, the evaluation is numerically reduced to matrix products, for which the most efficient routine are at hand.

To find to ground state now is just a matter of defining cleverly the variational algorithm which starts from random state $|\Psi\rangle$ and progressively goes down to the ground state. To this end, a Lagrange multiplier λ is introduced and $\langle\Psi|H|\Psi\rangle - \lambda\langle\Psi|\Psi\rangle$ is extremized. After some tedious but straightforward calculations [46], one arrives at a generalized eigenvalue problem of matrix dimension $dD^2 \times dD^2$ near every bond of the lattice. If dimension if still too large for exact diagonalization, the Lanczos algorithm can be used to find the lowest eigenvalues and eigenvectors.

This procedure is first carried on a the first bond, which modifies the matrix A^{σ_1}. It is then carried on iteratively along the lattice until the last site, and then backward, until convergence. Each passage throughout the lattice, in one sense or the other, is called a *sweep*. Convergence is achieved when the energy becomes constant, but other, more precise tests are possible, such as the convergence of $\langle\Psi|H^2|\Psi\rangle - (\langle\Psi|H|\Psi\rangle)^2$, see [46]. Moreover, improvement can be brought to the procedure by, for example, multiple sites variation, instead on variations on only one site.

The drawbacks are the usual ones met with variational problems: since the initial state is random, many sweeps will be required. However, this is overcame with a good initial guess, not too far from the true ground state. Another pitfall is to reach a local minimum instead of a global minimum; in [46, 53] this question is addressed in detail.

The truncation D has to be chosen carefully. For bosons, the situation is simplified if a constraint on the maximum number of particle per site can be set. Figure 3.1 shows the probability to find 0 to 3 particles at the middle site of the lattice in the Bose-Hubbard model (see chapter 2). These plots were obtained by DMRG with a constraint $N_{\max} = 8$, which is considered as large. In the Mott-insulating state (right side of the vertical line), clearly $N_{\max} = 4$ can be set. Unfortunately, it is not acceptable in the superfluid state. The interaction creates a natural limit on the number of particles per site; therefore, the case $U/J = 0$ is the most difficult for DMRG.

Thus, when doing ground-state calculations with DMRG, the main convergence parameter is the truncation D. For bosonic systems, another parameters, $N_{\max}$, naturally arises. If both parameters are well-controlled, DMRG is a extremely powerful algorithm.

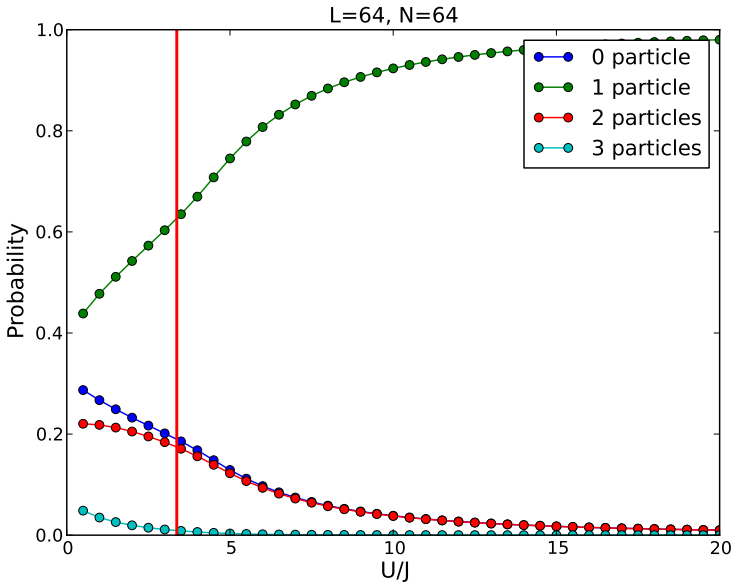

Figure 3.1: Probability to find 0,1,2 or 3 particles at middle site, versus the interaction strength U, for a commensurate filling, $\bar{n} = 1$. As soon as $U/J \geq 10$, the probability to find exactly one particle per site hit 0.9. By contrast, 3 and more particle per site are found with a probability smaller than $10e^{-3}$. This probability become appreciable in the superfluid phase. For $U/J = 0$, every occupation number is equally likely.

3.1.5 Time Evolution with MPS

Having a given state $|\Psi\rangle$ in a MPS form, for example the ground state of some H' Hamiltonian, its time-evolution is $e^{-iHt}|\Psi(0)\rangle$, where H is the Hamiltonian of the system. The matter is now the classical problem of applying the exponential of an operator.

The first step is to disretize time in T time-steps τ. Next, we split the Hamiltonian into two parts, H_{odd} and H_{even}, corresponding respectively to odd and even bonds. A popular way is to use the Trotter-Suzuki decomposition [38, 39]. At second order, it is:

$$e^{-iH\tau} = e^{-iH_{\text{odd}}\frac{\tau}{2}} e^{-iH_{\text{even}}\tau} e^{-iH_{\text{odd}}\frac{\tau}{2}} + \mathcal{O}(\tau^3). \tag{3.1}$$

A first control parameter is therefore the time-step. In general the error grows linearly with time as $\tau^n t$ where n is the order of the Trotter-Suzuki decomposition [38].

Secondly, after each time step, the evolved state is truncated so as to adapt continuously the Hilbert space to the state, instead of keeping the basis of the initial state. The Hilbert space follows the time-evolution of $|\Psi(t)\rangle$ (*adaptive* t-DMRG, see [7, 28]). Thus, convergence depends on a second control parameter. In practice, after truncation, the wavefunction has norm less than one and has to be renormalized. It is not easy in general to know how both errors combine and accumulate. In [18], a survey on a spin system which time-evolution can be calculated exactly was led, and the authors found that error at small times are dominated by the Trotter decomposition. However, the truncation error grows exponentially with time and eventually destabilizes the whole system. Inconsistent results are found after this "runaway" time, but the deviation from analytical results starts before.

Therefore, the time-step τ and the number of retained states should be chosen with a particular care. Several simulations should be led in parallel with different sets of control parameters. Depending on the purpose (long or short final times), the optimal parameters are not the same: a time-step too small may increase dramatically the truncation error and plague the simulation before the targeted final time. However, with sufficient attention, DMRG is efficient in time-evolution as well as in ground state calculations.

3.2 Dynamics: Perturbative Evolution of an Atomic Mott State

In section 2.1, we already introduced the notion of "atomic" Mott state. This is a product state with integer filling. All particles are localized and cannot move across the lattice. This is an ideal state, where the optical lattice height is infinite, and cannot be realized experimentally. The hopping J is introduced perturbatively, or, equivalently, the lattice height is lowered, toward strong but finite interaction.

The aim of this part is to calculate the evolution of an atomic Mott state under the Hamiltonian after the quench, written with U_{final}. In the Schrödinger picture, this is:

$$|\Psi(t)\rangle = \sum_p \exp(-itE_p)\langle\phi_p|\Psi(0)\rangle|\phi_p\rangle, \tag{3.2}$$

where $|\Psi(0)\rangle$ is the initial atomic Mott state, and $|\phi_p\rangle$ the eigenbasis of the new Hamiltonian, with eigenenergies E_p. We determine $|\phi_p\rangle$ and E_p by first-order perturbation in J/U. A similar approach were done in [9, 4], which relied on Jordan-Wigner fermionized quasiparticles. They managed to reproduce the behavior of the one-body correlation function $\langle a_0^\dagger a_d\rangle$, in good agreement with experimental data, down to $U/J \approx 15$. Propagation velocities were extracted.

On our side, we focus on the momentum distribution n_k, in order to gain insight into the dynamics of quasiparticles which takes place after the quench.

3.2.1 Perturbed Ground State and Excited States

The atomic Mott state is represented by the product state:

$$|\Psi(t \leq 0)\rangle = |\bar{n}, \bar{n}, ..., \bar{n}\rangle := |\bar{n}\rangle,$$

where $\bar{n}$ is the integer filling. Here, we focus on the case $\bar{n} = 1$, although our approach stands for any other integer values. As we lower U by the quench, the ratio U/J decreases but remains much larger than 1, allowing to introduce an hopping term,

$$T = -\sum_i (a_i^\dagger a_{i+1} + a_{i+1}^\dagger a_i)$$

as a perturbation:

$$H = \frac{U}{2}\sum_i n_i(n_i - 1) + JT = V_{\text{interaction}} + JT.$$

In this picture, an excitation consists in removing one particle from a given site (with therefore occupation $\bar{n}-1$), and placing it elsewhere on the lattice, on top of another particle (in total $\bar{n}+1$ on this site). In this process a hole-doublon pair is created, lying in the first excited band of energy U. Such pair can be denoted $|\phi^{(0)}_{m,d}\rangle$, and defined as:

$$|\phi^{(0)}_{m,d}\rangle = \frac{a_{m+d}a^\dagger_m}{\sqrt{\bar{n}(\bar{n}+1)}}|\bar{n}\rangle,$$

with $d \neq 0$. It describes the transfer of *only one* particle from site m to site $m+d$ within the chain. These states are normalized. Of course the hole and particle annihilates when they are placed on the same site; therefore the constraint $d \neq 0$ is introduced. This lowers the dimension of the excited basis to $L(L-1)$ (L choices for the hole, $L-1$ for the doublons, because the hole must remain), which is still highly degenerate.

To simplify the calculation, we restrict the spectrum of excitation to the first excited band. This amounts to treating the excitations as hardcore bosons, since we forbid more than two particles on the same site. However, to ensure that no information is lost, higher excitations are taken into account in a symbolic way: the next energy band has two doublons and two holes, at energy $2U$ with respect to the ground state. Thus, we introduce symbolically the states:

$$|\psi_{m,d,n,e}\rangle = \frac{a_{m+d}a_{n+e}a^\dagger_m a^\dagger_n}{\bar{n}(\bar{n}+1)}|\bar{n}\rangle,$$

with the constraint $m \neq n$, $d, e \neq 0$ $m+d \neq n+e$. This states describes two doublons and two holes located at four distinct positions. Because terms involving this state are only meant to ensure the correctness of the approximation, we will drop the indices of vector $|\psi\rangle$. We checked, when doing the time-evolution, that no terms involving these higher excitation are present at first-order in J/U.

Let us now calculate precisely the perturbed ground state. At first-order [3]:

$$|\Psi(0)\rangle = |\bar{n}\rangle - J\sum_{m,d}\frac{\left\langle\phi^{(0)}_{m,d}|T|\bar{n}\right\rangle}{E_0 - E_{m,d}}|\phi^{(0)}_{m,d}\rangle$$

For convenience, we wrote E_0 for the energy of state $|\bar{n}\rangle$, and $E_{m,d}$ for the energy of the state $|\phi^{(0)}_{m,d}\rangle$. Moreover, we already anticipated that $\langle\bar{n}|T|\bar{n}\rangle = 0$. The denominators are indeed U, the energy gap between the ground state and the first excited state, and the sums read:

$$\begin{aligned}
\sum_{m,d}\left\langle\bar{n}|a_m a^\dagger_{m+d}T|\bar{n}\right\rangle|\phi^{(0)}_{m,d}\rangle &= \sum_{m,d,n}\left\langle\bar{n}|a_m a^\dagger_{m+d}(a^\dagger_n a_{n+1} + a^\dagger_{n+1}a_n)|\bar{n}\right\rangle|\phi^{(0)}_{m,d}\rangle \\
&= \sqrt{\bar{n}(\bar{n}+1)}\sum_{m,d,n}(\delta_{n+1,m+d}\delta_{n,m} + \delta_{n,m+d}\delta_{n+1,m})|\phi^{(0)}_{m,d}\rangle \\
&= \sqrt{\bar{n}(\bar{n}+1)}\sum_{m}(\delta_{1,d} + \delta_{-1,d})|\phi^{(0)}_{m,d}\rangle.
\end{aligned}$$

The coefficient is $\sqrt{\bar{n}(\bar{n}+1)}$ since a doublon is first suppress and a hole is then filled.

In conclusion the perturbed ground state reads,

$$|\Psi(0)\rangle = |\bar{n}\rangle + \frac{J}{U}\sqrt{\bar{n}(\bar{n}+1)}\sum_m (|\phi^{(0)}_{m,+1}\rangle + |\phi^{(0)}_{m,-1}\rangle) \tag{3.3}$$

In the same fashion we may calculate the correction to the excited states; however, since excitations are degenerate, we have to take this degeneracy into account. To this end, we first perform a Fourier transformation of $|\phi_{m,d}\rangle$:

$$|\phi^{(0)}_{k,q}\rangle \propto \sum_m \sum_d \exp(ikm)\sin(dq)|\phi^{(0)}_{m,d}\rangle. \tag{3.4}$$

One can show that the kinetic (hopping) operator T is diagonal in this basis. Here a sinus is used instead of a complex exponential so as to take into account the constraint $d \neq 0$. Next we restrict ourself to the $k = 0$ component, to remain in the same symmetry sector as the initial state.

We have, writing $q = p\pi/L$, with p ranging from 1 to $L-1$, the relation :

$$\sum_d \sin\left(\frac{p\pi d}{L}\right)\sin\left(\frac{q\pi d}{L}\right) = \delta_{p,q}\frac{L}{2},$$

making the Fourier basis an orthonormal set. This property simplifies the treatment of the degeneracy, because it implies:

$$\begin{aligned}
J\left\langle \phi^{(0)}_p|T|\phi^{(0)}_q\right\rangle &= \frac{2J}{L^2}\sum_{m,d,m',d',n}\sin\left(\frac{dp\pi}{L}\right)\sin\left(\frac{d'q\pi}{L}\right)\left\langle \phi^{(0)}_{m,d}|(a^\dagger_n a_{n+1} + a^\dagger_{n+1}a_n)|\phi^{(0)}_{m',d'}\right\rangle \\
&= \frac{2J}{L}(2\bar{n}+1)\sum_d \sin\left(\frac{dp\pi}{L}\right)\sin\left(\frac{(d+1)p\pi}{L}\right) + \sin\left(\frac{dp\pi}{L}\right)\sin\left(\frac{(d-1)p\pi}{L}\right) \\
&= \frac{4J}{L}(2\bar{n}+1)\cos\left(\frac{p\pi}{L}\right)\sum_d \sin\left(\frac{dp\pi}{L}\right)\sin\left(\frac{dq\pi}{L}\right) \\
&= 2J(2\bar{n}+1)\cos\left(\frac{p\pi}{L}\right)\delta_{p,q}.
\end{aligned}$$

Now, the perturbed excited state is, at first-order:

$$|\phi_p\rangle = |\phi^{(0)}_p\rangle - J\frac{\left\langle \bar{n}|T|\phi^{(0)}_p\right\rangle}{E_p - E_0}|\bar{n}\rangle - J\sum_k \frac{\left\langle \psi_k|T|\phi^{(0)}_p\right\rangle}{E_p - E_k}|\psi_k\rangle.$$

Above, we have:

$$\begin{aligned}
\frac{L}{\sqrt{2}}\left\langle \bar{n}|T|\phi^{(0)}_p\right\rangle &= \sum_{m,d,n}\sin\left(\frac{dp\pi}{L}\right)\left\langle \bar{n}|(a^\dagger_n a_{n+1} + a^\dagger_{n+1}a_n)a_{m+d}a^\dagger_m|\bar{n}\right\rangle \\
&= \sqrt{\bar{n}(\bar{n}+1)}L\left(\sin\left(\frac{p\pi}{L}\right) + \sin\left(\frac{(L-1)p\pi}{L}\right)\right).
\end{aligned}$$

Therefore:

$$J\frac{\left\langle \bar{n}|T|\phi_p^{(0)}\right\rangle}{E_p - E_0} = \frac{J}{U}\sqrt{2\bar{n}(\bar{n}+1)}(1-\cos(p\pi))\sin\left(\frac{p\pi}{L}\right).$$

We will use the notation $\eta_p = 1 - \cos(p\pi)$. In conclusion,

$$|\phi_p\rangle = |\phi_p^{(0)}\rangle - \frac{J\sqrt{2\bar{n}(\bar{n}+1)}}{U}\eta_p \sin\left(\frac{p\pi}{L}\right)|\bar{n}\rangle - \frac{J}{U}\sum_k \beta_k|\psi_k\rangle, \tag{3.5}$$

where $\beta_k = \left\langle \psi_k|T|\phi_p^{(0)}\right\rangle$ is kept symbolic.

Finally, we need the eigenenergies of the perturbed states. With respect to the unperturbed ground state energy (which would result in an overall unimportant phase factor):

$$\begin{aligned} E_0 &= 0, \\ E_p &= U - J\left\langle \phi_p^{(0)}|T|\phi_p^{(0)}\right\rangle \\ &= U - 2J(2\bar{n}+1)\cos\left(\frac{p\pi}{L}\right). \end{aligned}$$

In the second equation, we used:

$$\sum_p \eta_p^2 \sin^2\left(\frac{p\pi}{L}\right) = L.$$

At this point, we know the perturbed ground state and excited states, as well as their respective energies. The time evolution is then simply obtained from 3.2, what we do in the following section.

3.2.2 Time Evolution of the Atomic Mott State

As mentioned, the time evolution is found by (3.2):

$$|\Psi(t)\rangle = e^{-iE_0 t}|\Psi(0)\rangle + \sum_{p=1}^{L-1}\frac{J}{U}e^{iE_p t}|\phi_p\rangle, \tag{3.6}$$

where $|\Psi(0)\rangle$ is the perturbed ground state and $|\phi_p\rangle$ the lowest band of excited state, of energy E_p, obtained in the previous section. Replacing and neglecting terms in $(J/U)^n$ with $n \geq 2$ (because we want a first-order expansion), this reads:

$$|\Psi(t)\rangle = |\bar{n}\rangle + \frac{J\sqrt{\bar{n}(\bar{n}+1)}}{U}\left(\sum_m(|\phi_{m,+1}^{(0)}\rangle + |\phi_{m,-1}^{(0)}\rangle) - \sqrt{2}\sum_p e^{-iE_p t}\eta_p \sin\left(\frac{p\pi}{L}\right)|\phi_p^{(0)}\rangle\right). \tag{3.7}$$

Note that, at $t = 0$, second and third terms cancel each other, so that we recover $|\Psi(0)\rangle = |\bar{n}\rangle$. Moreover, no term involving the second band appear, because a factor J^2/U^2 would weight them. With this state in hand, we can calculate expectation values of the relevant observables.

3.2.3 Equal-Time Correlation Function

An mentioned in the introduction, we are mainly interested in one-body correlations,

$$C_r(t) = \left\langle \Psi(t) | a_0^\dagger a_r | \Psi(t) \right\rangle .$$

Replacing with the state $|\Psi(t)\rangle$ obtained in the previous section, we have at first-order in J/U:

$$C_r(t) = \frac{J\sqrt{\bar{n}(\bar{n}+1)}}{U} \left(\sum_m \left\langle \bar{n} | a_0^\dagger a_r | \phi^{(0)}_{m,+1} \right\rangle + \left\langle \bar{n} | a_0^\dagger a_r | \phi^{(0)}_{m,-1} \right\rangle \right.$$
$$\left. - \sqrt{2} \sum_p \eta_p \sin\left(\frac{p\pi}{L}\right) e^{-iE_p t} \left\langle \bar{n} | a_0^\dagger a_r | \phi^{(0)}_p \right\rangle \right) + \text{h. c.}.$$

In this expression,

$$\sum_m \left\langle \bar{n} | a_0^\dagger a_r | \phi^{(0)}_{m,+1} \right\rangle + \left\langle \bar{n} | a_0^\dagger a_r | \phi^{(0)}_{m,-1} \right\rangle + \text{h. c.} = 2\sqrt{\bar{n}(\bar{n}+1)}\delta_{r,1}$$

and:

$$\left\langle \bar{n} | a_0^\dagger a_r | \phi^{(0)}_p \right\rangle + \text{h. c.} = \frac{2}{L}\sqrt{2\bar{n}(\bar{n}+1)} \sin\left(\frac{p\pi}{L}\right).$$

In conclusion,

$$C_r(t) = \frac{2J\bar{n}(\bar{n}+1)}{U} \left(\delta_{r,1} - \frac{2}{L} \sum_p \cos\left(Ut - 2J(2\bar{n}+1)\cos\left(\frac{p\pi}{L}\right) t \right) \eta_p \sin\left(\frac{p\pi}{L}\right) \sin\left(\frac{rp\pi}{L}\right) \right). \tag{3.8}$$

Remark that $C_r(t=0) = 0$; for $r = 1$, the second term exactly cancels the first. In the next chapter this formula will be confronted to DMRG data.

3.2.4 Momentum Distribution

We now turn to the other quantity of interest, the momentum distribution. From the definition 2.5 (neglecting the enveloping Wannier function w and also the normalization $\bar{n}$), we have:

$$\begin{aligned} n_k &= \sum_{d=0}^{L} 2\cos(dk) \langle a_0^\dagger a_d \rangle \\ &= \bar{n} + \frac{4J\bar{n}(\bar{n}+1)}{U} \times \\ &\left(\cos(k) - \frac{2}{L} \sum_p \cos\left(Ut - 2J(\bar{n}+1)\cos\left(\frac{p\pi}{L}\right) t \right) \eta_p \sin\left(\frac{p\pi}{L}\right) \sum_d \cos(dk) \sin\left(\frac{dp\pi}{L}\right) \right), \end{aligned}$$

where $\eta_p = 1 - \cos(\pi p)$.

As mentioned in the previous chapter, the $n_k - \bar{n}$ shows a peak at $k = 0$ in the superfluid state, whereas a value close to zero in the Mott-insulating state. This peak is

a signature of the coherence which exists on the lattice. Therefore, we give here an exact formula for $k = 0$. The second sum is given by the Lagrange identity:

$$\sum_{d=1}^{L} \sin(d\theta) = \frac{1}{2\tan(\theta/2)} - \frac{\cos((L+1/2)\theta)}{2\sin(\theta/2)} := \mathcal{L}(\theta),$$

where $\theta = \frac{p\pi}{L}$. Therefore,

$$n_0 = \bar{n} + \frac{4J\bar{n}(\bar{n}+1)}{U}\left(1 - \frac{2}{L}\sum_p \cos\left(Ut - 2J(\bar{n}+1)\cos\left(\frac{p\pi}{L}\right)t\right)\eta_p \sin\left(\frac{p\pi}{L}\right)\mathcal{L}\left(\frac{p\pi}{L}\right)\right). \tag{3.9}$$

Thus, a nice expression for the momentum distribution can be obtained for every k, with a further simplification for $k = 0$ where only one sum over an additional quantum number, p, remains. This number should be thought as the Fourier transform of the distance separating a doublon and a hole. Before we compare this formula with the DMRG data, a last observable can also be of great help: the time-averaged value of the momentum distribution, $\langle n_k \rangle_t$.

Through averaging, the time-dependent part of n_k vanishes, and there remains, at first-order:

$$\langle n_k \rangle_t = \bar{n} + \frac{4J\bar{n}(\bar{n}+1)}{U}\cos(k) + \mathcal{O}\left(\frac{J^2}{U^2}\right)$$

In particular, for $k = 0$, we simply find:

$$\langle n_0 \rangle_t = \bar{n} + \frac{4J\bar{n}(\bar{n}+1)}{U}. \tag{3.10}$$

For $k = \pi/2$, the first-order contribution vanishes, and in our approximation $\langle n_{\pi/2} \rangle_t$ should be zero. However, as said only constant terms will contribute here. Coming back to (3.7), one sees that the only constant second-order terms arise from the overlap between the second term with itself, and the first ($|\bar{n}\rangle$) with a J^2/U^2 term, absent above. However, the former results of the application of T on $|\phi^{(0)}_{m,\pm 1}\rangle$. It will describe excitations with 2 holes and 1 triplon, two doublon-hole pairs separated on the lattice (where, in each, doublon and hole are nearest-neighbor), or a back-scattering to the initial state, $|\bar{n}\rangle$ (annihilation of the pair). But the application of $a_0^\dagger a_d$ to any of these three cases yields states which are orthogonal to $|\bar{n}\rangle$.

Therefore, the only contributing terms will be:

$$\frac{J^2\bar{n}(\bar{n}+1)}{U^2}\left(\sum_m \left\langle \phi^{(0)}_{m,-1}|a_0^\dagger a_d|\phi^{(0)}_{m,+1}\right\rangle + \left\langle \phi^{(0)}_{m-1,+1}|a_0^\dagger a_d|\phi^{(0)}_{m+1,-1}\right\rangle + \text{h. c.}\right)$$

The first (second, its hermitian conjugate) term describes the displacement of a hole by two sites leftwards (rightwards), the third (fourth) of a doublon by two sites rightwards (leftwards). Thus, as expected from second-order, only $d = 2$ terms are non-zero.

Then, with $n_{\pi/2} = \sum_d \cos(d\pi/2)\langle a_0^\dagger a_d \rangle$, we obtain:

$$\langle n_{\pi/2} \rangle_t = \bar{n} - \frac{4J^2\bar{n}(\bar{n}+1)(2\bar{n}+1)}{U^2}. \tag{3.11}$$

As the next chapter demonstrates, both approximations produce accurate results down to $U/J \approx 10$.

3.2.5 Quench to $U/J = 0$

As shown in [4, 16], the extreme quench to zero interaction is exactly solvable by working in the Heisenberg picture, where the time evolution of the annihilation operator is written as:

$$a_m(t) = \sum_{l=1}^{L} V_{m,l}(t) a_l, \tag{3.12}$$

with the free particle propagator:

$$V_{m,m+r}(t) = \frac{1}{2\pi} \int_{-\pi}^{\pi} e^{-i(2J\cos(\phi)t - r\phi)} \mathrm{d}\phi = i^r \mathcal{J}_r(2Jt). \tag{3.13}$$

J_r is the Bessel's function of the first kind.

With this expression correlations can be derived (recall we have $\hbar = 1$),

$$\begin{aligned} C_r &= \left\langle \bar{n} | a_0^\dagger(t) a_d(t) | \bar{n} \right\rangle \\ &= \sum_{m,l} V_{0,m}^\dagger(t) V_{d,l}(t) \left\langle \bar{n} | a_m^\dagger a_l | \bar{n} \right\rangle \\ &= \bar{n} \sum_m V_{0,m}^\dagger(t) V_{d,m}(t) = \bar{n} \sum_m V_{0,m}^\dagger(t) V_{0,m-d}(t) \\ &= \bar{n} \sum_m i^{m-d} (-i)^m \mathcal{J}_m(2Jt) \mathcal{J}_{m-d}(2Jt). \end{aligned}$$

From this expression it is possible to get an analytical formula for n_k also.

In the next chapter, we base an analysis of the non-equilibrium quantum many-body state produced by the quench on the perturbative expressions for the one-body correlations and the momentum distribution obtained in this chapter. This will allow us to understand the structure of this state, and in particular its coherence.

Chapter 4

Dynamics with a Mott Insulator Ground State

In this chapter, the effects of a quench in U/J on a atomic Mott state are investigated. Although the initial state is particularly simple, these effects are not easily described, and the system is driven by an interesting dynamics. After the quench, a quasiparticle is created and propagates. It can be neatly seen as a wavepacket, which is a superposition of oscillations at different frequencies. We show that, down to $U/J \approx 20$, the perturbation theory developed in the previous chapter allows to understand the structure of this quasiparticle by revealing which frequencies are most important. This is discussed in section 4.1, where a propagation velocity is also extracted. The velocity is found asymptotically independent of the final ratio U/J, in agreement with [9].

Next, in section 4.2, the momentum distribution is studied. It provides information about the coherence of the atomic cloud, which is found enhanced after the quench. This can be understood as a coherent superposition of quasiparticles. When U/J is lowered, more and more quasiparticles are created and the coherence grows correspondingly. Perturbation theory predicts a power-law scaling, and it is close to the correct result, but a discrepancy is observed for U/J smaller than approximately 5.5. There, coherence is destroyed because the excitations are too strong, and the system enters a new regime where the quasiparticle picture does not hold anymore.

4.1 Spreading of Correlations after a quench

We start by a brief study of the evolution of the one-body correlation function $\langle a_0^\dagger a_d \rangle$. The quench is performed on an atomic Mott state,

$$|\Psi(0)\rangle = \bigotimes_{i=1}^{L} |\bar{n}\rangle,$$

with a filling $\bar{n} = 1$. Therefore, unlike section 2.4, the initial state is unique and not a complicated superposition of many states. As a consequence, $\langle a_0^\dagger a_r \rangle$ looks less noisy, and it will be easier to extract the velocity.

As figure 4.1 (a) shows, for a quench to $U/J = 60$, the correlations spread in a wavepacket. Its internal frequency is close to $2\pi/U$ (see below) and, at first glance,

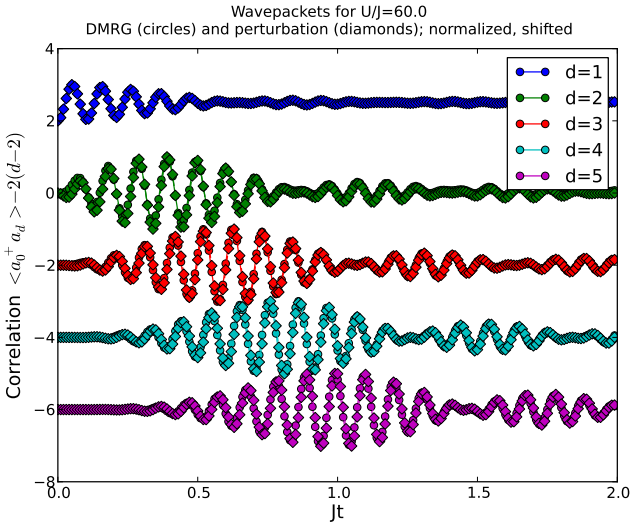

(a)

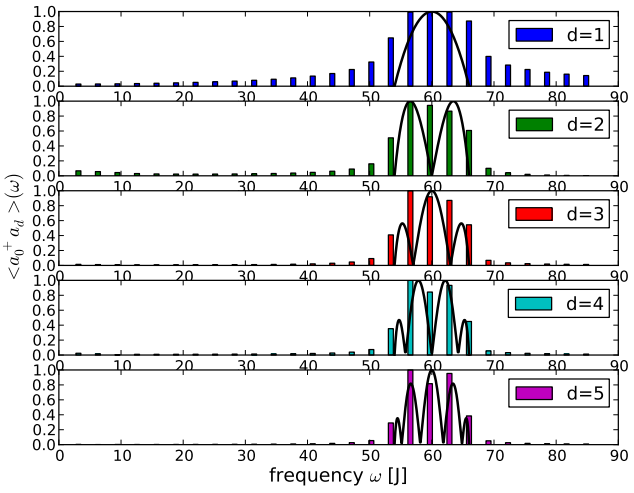

(b)

Figure 4.1: (a) Correlation function $\langle a_0^\dagger a_d \rangle$ for $U/J = 60$ and $d = 1$ to 5, versus time. Circles mark DMRG, squares the first-order perturbation formula, equation (4.1) Each curve is normalized to one and shifted below the previous one for clarity. This emphasizes the propagation of a wavepacket. A principal wavepacket can be seen, between $0 < t < 0.80$ for $d = 2$ for example. Additionally, a second and third wavepackets, of smaller amplitudes, can be seen between $0.9 < t < 1.4$ and $1.5 < t < 1.75$ for the same d. (b) Fourier transform of the curves in (a). The bars is the Fourier transform of the DMRG data, and the black curves indicates the frequencies ω predicted by perturbation theory, weighted by a prefactor (see text). DMRG shows a bandwidth which is well reproduced by perturbation, except for $d = 1$, where is is underestimated. For even d, a frequency at $\omega = U = 60J$ is suppressed by perturbation. For the other distances the agreement is good.

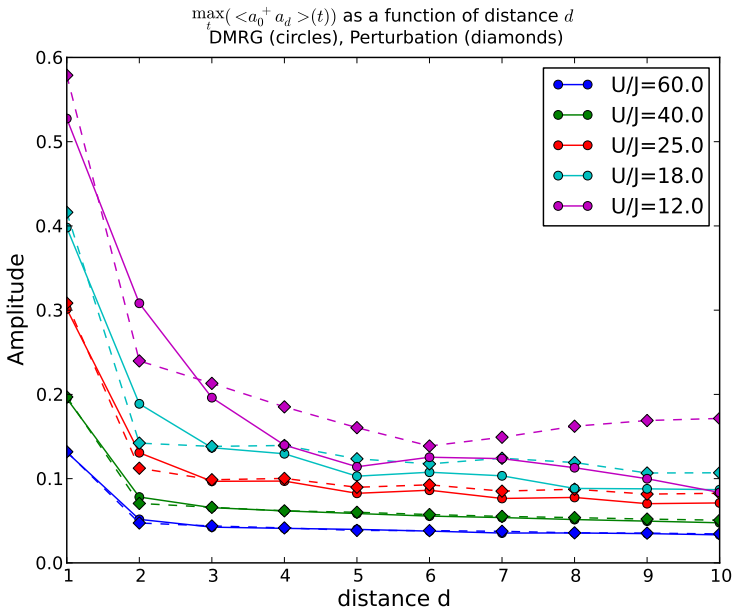

Figure 4.2: Maximum amplitude reached by one-body correlations $\langle a_0^\dagger a_d \rangle$ in the times $0 < Jt < 2$, as a function of d for several final U/J. The DMRG data is in plain line with circle marker, the perturbation theory results in dashed line with diamond marker. The point $d = 1$ has a larger amplitude, because nearest-neighbor tunelling is the leading process in the Bose-Hubbard Hamiltonian. For large U/J and $d > 1$, the decrease is linear and slow. As U/J is lowered, small amplitude oscillations are observed. The perturbation deviates for $U/J < 20$.

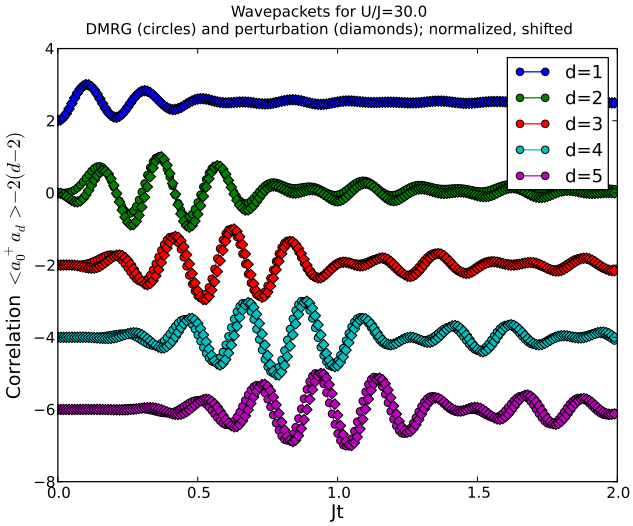

(a)

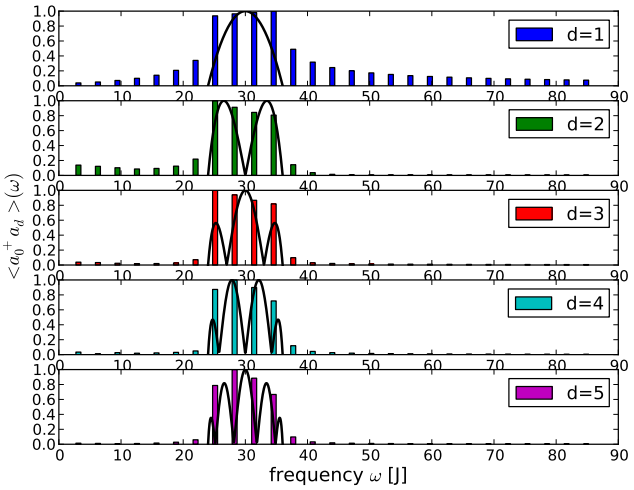

(b)

Figure 4.3: Same as figure 4.1, with $U/J = 30$. In (a), the agreement between DMRG data (circles) and perturbation theory (diamonds) is still very well for $\langle a_0^\dagger a_d \rangle$. Similarly, in (b), the frequency bands are well covered by the frequencies extracted from (4.1), but the weight associated with each frequency may not be correct. With the current precision of DMRG, it is not possible to validate such predictions.

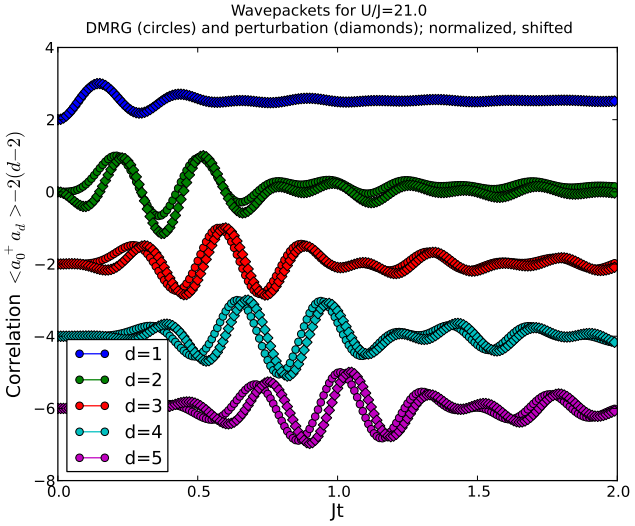

(a)

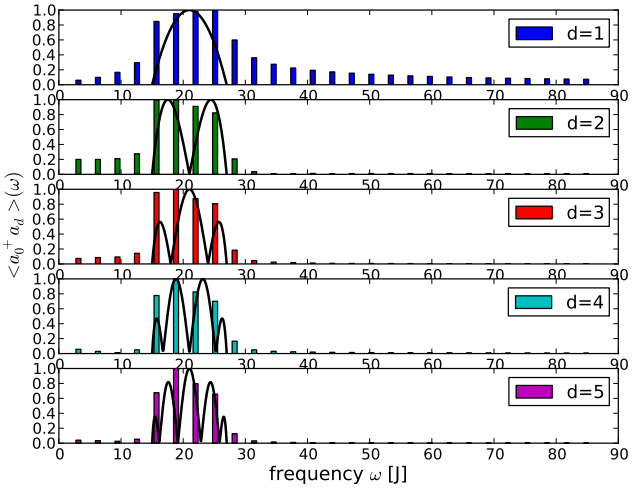

(b)

Figure 4.4: Same as figure 4.1, with $U/J = 21$. The comments of figures 4.1 and 4.3 still apply here.

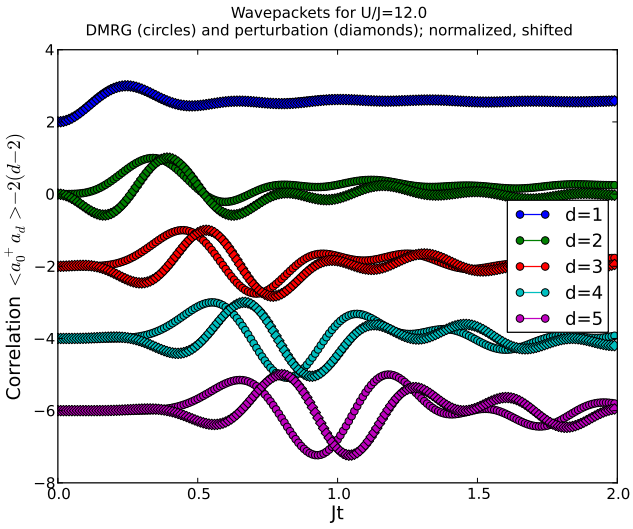

(a)

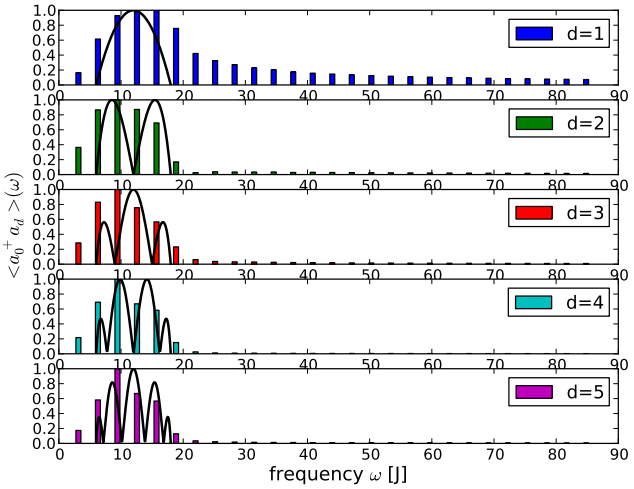

(b)

Figure 4.5: Same as figure 4.1, with $U/J = 12$. (a) For $\langle a_0^\dagger a_d \rangle$ the perturbation begins to overestimate the speed of propagation: except for $d = 1$ the fronts are in advance over the DMRG data. This worsens with the distance. (b) A discrepancy between DMRG and perturbation can be seen: the predicted bandwidth is shifted toward large frequencies, which results in the advance seen in (a).

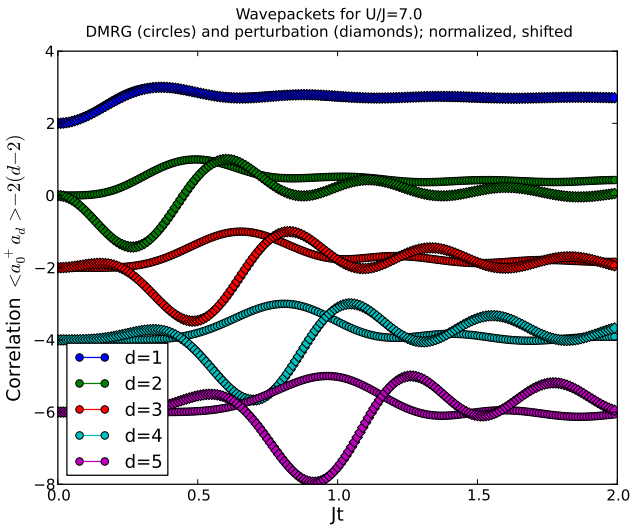

(a)

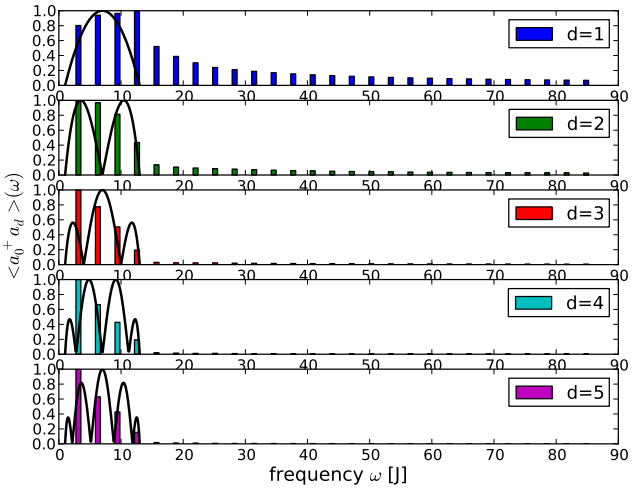

(b)

Figure 4.6: Same as figure 4.1, with $U/J = 7$. (a) In this case the first-order perturbation fails completely, except for $d = 1$. For other distances oscillations are predicted, but $\langle a_0^\dagger a_d \rangle$ reaches a plateau, which is vaguely reproduces by the perturbation. But the arrival of the signal is missed, meaning the quasiparticle is not correctly described. (b) Frequencies close to $\omega = 0$ are becoming important. Though with formula (4.2) it is possible to reach $\omega/J = 1$ for $U/J = 7$, low frequencies are suppressed by the prefactor. A second-order treatment may improve this.

the velocity of the propagating front seems linear. However, the exact shape of the wavepacket varies with distance: 10 peaks can be seen for $d = 6$, but only 7 at $d = 2$. Thus the wavepacket flattens with the distance: its width grows and its amplitude (maximum height reached in time) decays slightly. Figure 4.2 shows this attenuation with the distance, for several values of U/J. Moreover, the symmetry of the wavepacket decreases with the distance, and a tail can be seen.

All these phenomena are reproduced with a good accuracy by the perturbation formula obtained in the chapter 3.2.3,

$$\langle a_0^\dagger a_d \rangle = \frac{2J\bar{n}(\bar{n}+1)}{U} \left(\delta_{d,1} - \frac{2}{L} \sum_p \cos\left(Ut - 2J(2\bar{n}+1)\cos\left(\frac{p\pi}{L}\right) t \right) \eta_p \sin\left(\frac{p\pi}{L}\right) \sin\left(\frac{dp\pi}{L}\right) \right). \tag{4.1}$$

This formula also allows to catch the main structure of the wavepacket. To extract the main frequencies of the wavepackets, we plotted in figure 4.1 (b) the Fourier transform $\langle a_0^\dagger a_d(\omega) \rangle$. A band of frequency can be seen between $50J \leq \omega \leq 70J$. This can be understood with the formula 4.1: the time-dependent part of shows a superposition of cosines at frequencies:

$$\omega = U - 2J(2\bar{n}+1)\cos\left(\frac{p\pi}{L}\right), \tag{4.2}$$

where p is an integer running from 1 to L. This gives a frequency spectrum $U - 6J \leq \omega \leq U + 6J$, or, with $U/J = 60$, $54J \leq \omega \leq 66J$, in agreement with the DMRG data. These cosines are weighted by a p- and d-dependent factor. In 4.1 (b), we also plotted those frequencies, weighted by their prefactors, for every distance (black curves). It shows which frequencies are dominating, according to the perturbation theory. The prefactor can be rewritten as:

$$\sin\left(\frac{p\pi}{L}\right)\sin\left(\frac{dp\pi}{L}\right) = \frac{1}{2}\left(\cos\left(\frac{(d-1)p\pi}{L}\right) - \cos\left(\frac{(d+1)p\pi}{L}\right)\right)$$

For $d = 1$, for example, this is maximal at $p = \pm L/2$, that is, according to (4.2), $\omega = U$. This is simply the frequency obtained when $J = 0$, see chapter 2.4. However, the other frequencies are not suppressed, but weighted. This results in the bandstructure shown by the black curves in 4.1 (b). The true bandstructure (bars) is qualitatively reproduced, even if underestimated. Moreover, the weights are symmetric with respect to the frequency $\omega = U$, which is not the case in the DMRG data.

Similarly, for $d = 2$, the prefactor is maximal for $p = \pm L/3$, and therefore, two frequencies, $\omega \approx U \pm 3J$ will dominate. The bandwidth is again with a good presicion contained into the range of frequencies allowed by perturbation theory.

Continuing this way, we obtain the other black curves of figure 4.1 (b). For odd d, the first cosine above gives a dominant frequency at U, at $U \pm 6\cos\left(\frac{(d+1)\pi}{L}\right)$ for even d, with, in both cases, additional sub-frequencies. It is difficult, however, to reach with DMRG long enough a time to obtain a presition on ω comparable to what we can obtain in this approach. The border of the bands and their width are generally well reproduced, and this is in favor or our approach. It would be interesting to reach longer times with DMRG, so as to obtain a precision on ω which could allow a comparison with perturbative predictions.

How is this modified when U/J is decreased ? Figures 4.3 (a) to 4.6 (a) presents $\langle a_0^\dagger a_d \rangle$ for $d = 1$ to 5 and several values of the final U/J. The oscillations are fewer, indicating

a decrease of the frequency. When U/J is roughly smaller than 15, perturbation theory fails to catch this decrease, as (b) in those figures show. The bands do not fundamentally change, and the perturbation can still cover them, but the main frequencies are shifted toward low values. The bands are asymmetric, whereas the perturbation predicts a symmetry: $U + \alpha J$ and $U - \alpha J$ are always evenly weighted.

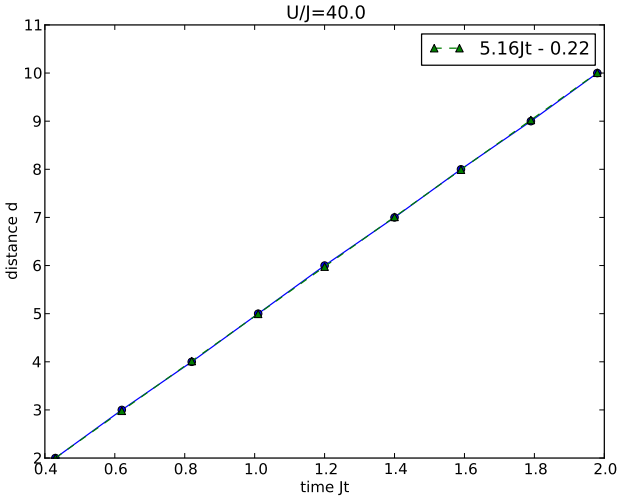

Figure 4.7: Linear fits of the DMRG data for the velocity of the propagating quasiparticle, with the formula $d = vt + v_0$, for $U/J = 40$. The d^{th} time is the one for which $\langle a_0^\dagger a_d \rangle$ is maximal.

An expending wavepacket exists down to $U/J \approx 5$. Thus, for these values of U/J, a velocity can clearly be defined. To extract it, we plot the time at which $\langle a_0^\dagger a_d \rangle$ reaches its maximum versus d. This gives for example the approximatively linear curve of figure 4.7. The slope of those curves provides a velocity, according to the formula $d = vt + d_0$. We find a velocity $v \approx 5.16J$ for $U/J = 40$. In general, it is not clear how the velocity depends on the final U/J [9] and the initial state. In our case, as indicated in figure 4.8, it does not seem to vary much with the final U/J.

In conclusion, $\langle a_0^\dagger a_d \rangle$ shows a clear behavior which allows to extract a propagation velocity. A nice interpretation in terms of a propagating wavepacket can be thought, with internal frequency close to the characteristic frequency $2\pi/U$ predicted by quantum mechanics. To the eye, only the amplitude of this wavepacket depends on the ratio U/J (figure 4.2), not its width nor group velocity. Thus, the velocity of the propagating front is roughly independent of the ratio U/J, at least in the range $U/J \geq 10$. This is not a peculiarity of the chosen initial state: in [4], with an initial ratio $(U/J)_{\text{initial}} = 40$, the velocity was found asymptotically equal to $6J$ when $U/J \to 40$ (figure 7 (c)), a value comparable to our $5.16J$.

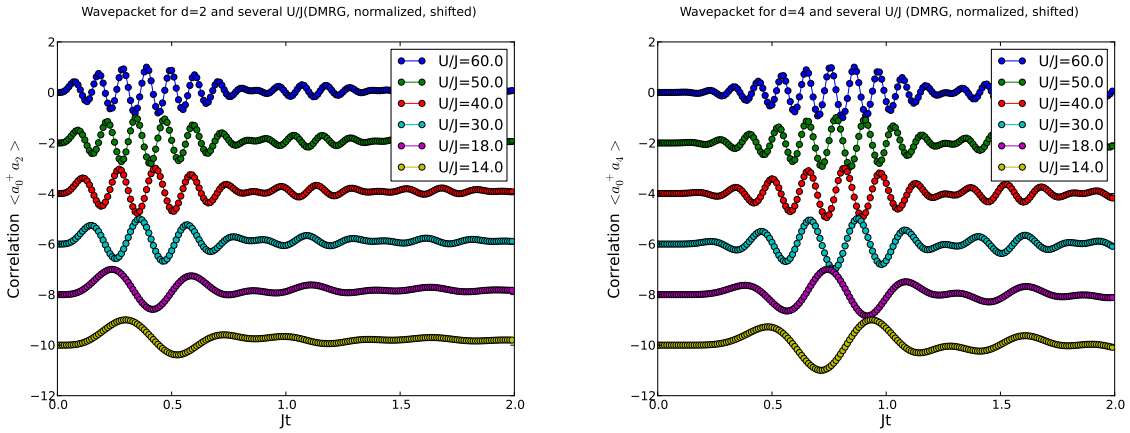

(a) d=2

(b) d=4

Figure 4.8: Wavepackets of the propagating quasiparticles. The shift of fast frequency is clear, but the whole wavepacket is not significantly shifted rightwards as U/J is lowered. As a result, its propagation velocity poorly depends on the interaction strength, at least in this range of final U/J.

4.2 Momentum Distribution

In the previous section, we saw that through the one-body correlations $\langle a_0^\dagger a_d \rangle$ the propagation of a wavepacket can be seen. This wavepacket can be though as a quasiparticle [4], a superposition of several excitations, or different doublon-hole pairs in the perturbation picture. The aim of this section is to understand in more detail which excitations are involved. To this aim, the momentum distribution will be the tool.

An overall view of the momentum distribution $n_k - \bar{n}$ is presented in figure 4.9, obtained from DRMG data. The first notable thing is the peak developing around $k = 0$ after $t \approx 2\pi/U$, where U is the final interaction strength. This peak is an excitation at small momentum. As time goes on, its amplitude seems to dicrease, and to be transferred to other momenta around $\pi/2$. Thus, other excitations are accessible to the system after the quench. In the first section, we focus on the spectrum of excitation at a large U/J, guided by the perturbation theory developed, which, as we explained in the previous section, can reproduce the quasiparticles with a good precision. Next, we lower the final U/J in order to see how this modifies the excitation spectrum.

4.2.1 Spectrum of excitation at $U/J = 50$

Let us start with the case $k = 0$. Figure 4.10 shows the evolution of $n_{k=0} - \bar{n}$. It presents fast oscillations of decreasing amplitude. An extrema is reached almost exactly after $\nu_0/2$, where $\nu_0 = 2\pi/50 \approx 0.125$ is the oscillation frequency neglecting completely hopping. The amplitude is decreasing afterwards rather quickly. Perturbation theory can help us to understand what happens.

Just as $\langle a_0^\dagger a_d \rangle$, we found in section 3.2.4 that the evolutionary part of n_k could be written as a superposition of cosines at frequency $\omega_p = U - 2J(2\bar{n}+1)\cos\left(\frac{p\pi}{L}\right)$, where p is an integer running from 1 to L. The weight, however, is not the same as in $\langle a_0^\dagger a_d \rangle$. It

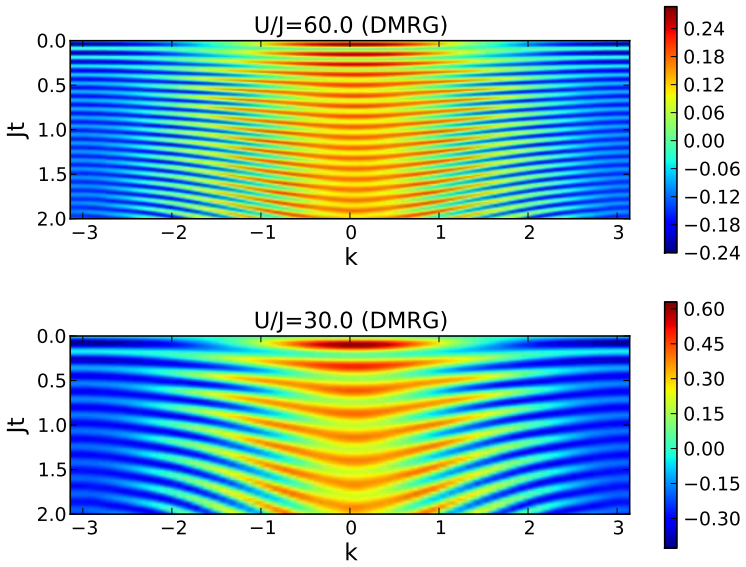

(a)

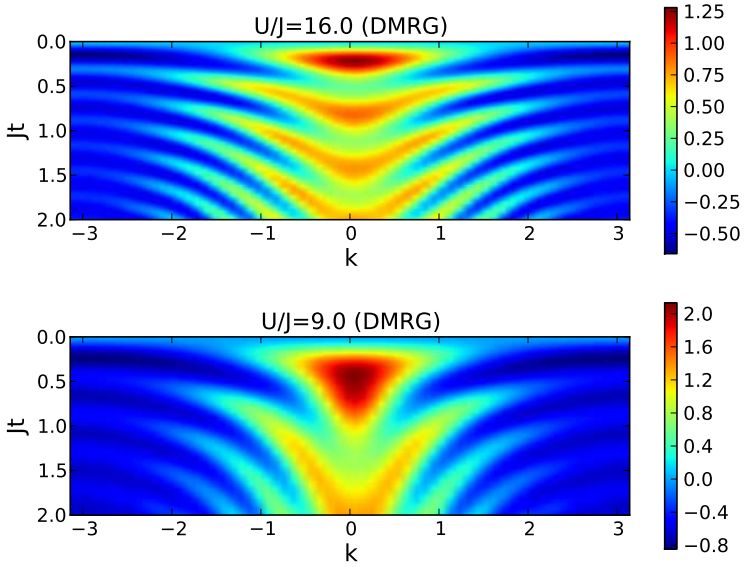

(b)

Figure 4.9: Color plot of the momentum distribution $n_k - \bar{n}$. From top to bottom: $U/J = 60, 30, 16, 9$. The time is shown in vertical axis, the momentum k in horizontal axis. Oscillation, fast in (a, top, $U/J = 60$), decreases with U/J. Whereas n_k is just $\bar{n}$ at $t = 0$ for any k a dependence on the momentum appears afterwards. The higher the momenta, the smaller the frequency, which results in the boomerang-shaped red areas.

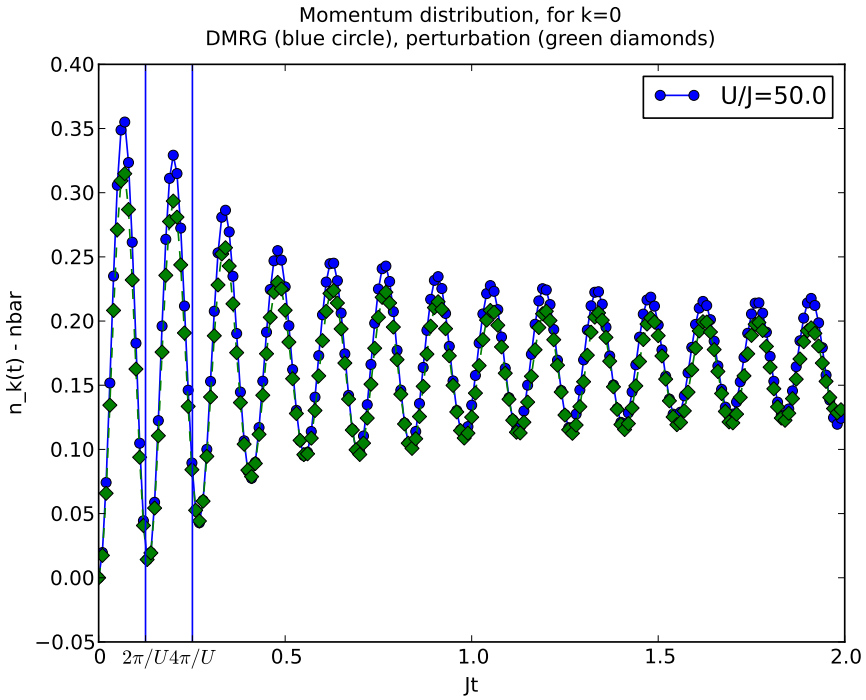

Figure 4.10: For $U/J = 50$, momentum distribution $n_{k=0} - \bar{n}$, perturbation (green, formula 3.9) and DMRG (blue). The two vertical blue lines are at $t = 2\pi/U = \nu_0$ and $t = 2\nu_0$, to indicate that the first period is indeed close to ν_0, which would be the period of oscillation without hopping. After two periods, though, the deviation is already appreciable, which means hopping is already acting (see also section 2.4 where the same phenomena occurs). The perturbation, in green, agrees very well. The maxima, however, are slightly underestimated.

is a k-dependent factor,

$$f(k,p) = \sum_d \cos(dk) \sin\left(\frac{dp\pi}{L}\right). \tag{4.3}$$

This is found to be dominant for $p\pi/L$ close to k, and decreasing fastly with the distance $|p\pi/L - k|$. Therefore, unlike the previous section, here we clearly identity one and only one main frequency,

$$\Omega_k = U - 2J(2\bar{n}+1)\cos\left(\frac{k\pi}{L}\right).$$

To understand deeper the structure of the curve 4.10, we plotted in the top part of figure 4.11 its Fourier transform. Besides the dominant frequency, a bandwidth can be seen. Both can be understood by the perturbation theory. In figure 4.12, we plotted the main expected frequency Ω_k (dashed line); it is found extremely close to the main DMRG frequency.

This proves that, for instance, for $k = 0$ (and $\bar{n} = 1$ to simplify), the main excitation carries a frequency ω of $U - 6J$. Similarly, at $k = \pi/2$, it will simply be U. Moreover, the decrease of the weight (4.3) is not the same for every k. It is decreasing almost linearly for $k = 0$ and $k = \pi$, but exponentially for intermediate frequencies. Although the DMRG data do not show such decrease, figure 4.12 shows that the bandwidths are qualitatively reproduced. What is more satisfying is the position of the main frequency, which is almost exactly the one predicted by perturbation theory.

We are now in position to study how individual momenta are excited after the quench. Figure 4.13 shows, for every time t, near which k the momentum distribution is maximal. Initially at $k = 0$, a competition with $k = \pi/2$ quickly appears, with a constant transfer of the maxima between the two values. This is the signature of the quasiparticle with one site between the hole and the doublon, because we have $n_{k=\pi/2} = -\langle a_0^\dagger a_2\rangle + \langle a_0^\dagger a_4\rangle + ...$, and presumably quasiparticles with larger distances between the hole and the doublon are not yet formed.

Moreover, the peak at $k = 0$ is not destroyed, its amplitude decreases, but the oscillations continue. This can be understood as a growth of coherence in the lattice. Examining figure 4.1 (a), we see that the quasiparticle $\langle a_0^\dagger a_1\rangle$ has not disappeared when $\langle a_0^\dagger a_2\rangle$ begins to oscillate. Excitations with zero and two sites between the hole and the doublon are superposed for a while, and this results in a double peaked momentum distribution, and therefore larger coherence. The wavepackets are not in phase, consequently the two peaks are not maximal at the same time, but the idea is clear.

As time goes on, the $k = 0$ momentum ceases to dominate, and, as figure 4.14 shows, when $t > 1.0J$, peaks at several intermediate momenta are appearing. They can not be directly associated with a precise doublon-hole pair, only with the superposition $\sum_d \cos(dk)\langle a_0^\dagger a_d\rangle$, and therefore these peaks indicate that a particular superposition of quasiparticles is taking place on the lattice. To see several peaks at the same time on the momentum distribution, as in figure 4.14, indicates a coherence between several superpositions of quasiparticles, something which was not obvious from the previous section, with the sole $\langle a_0^\dagger a_d\rangle$.

In conclusion, even with a trivial initial state –an atomic Mott state– and a high final interaction strength, the dynamic induced by the quench is rich and non-trivial. Elementary quasiparticles are forming coherent superpositions, and individually, each of them carries a different bandwidth. This bandwidth is the largest at low momenta, but persists for every k. Right after the quench, the small momenta components dominate, but quickly additional peaks can be seen, indicating an interplay between quasiparticles and a growth of coherence.

As we showed, very simple first-order perturbative calculations proved to be useful to catch the main structure of this dynamics. The main frequency of every quasiparticle can be very precisely found. The range of excitation frequencies is $U - 2J(2\bar{n}+1) \leq \omega \leq U + 2J(2\bar{n}+1)$, a width of $12J$ centered around U. A qualitative aspect of the bandstructure can also be extracted. Moreover, the analytical formula predicts, with a good accuracy up to times $t \sim 2J$, the evolution of every components of the momentum distribution, which may allow a deeper understanding of the coherent processes at work.

In the next section, we evaluate the effects of a larger final U/J on those results.

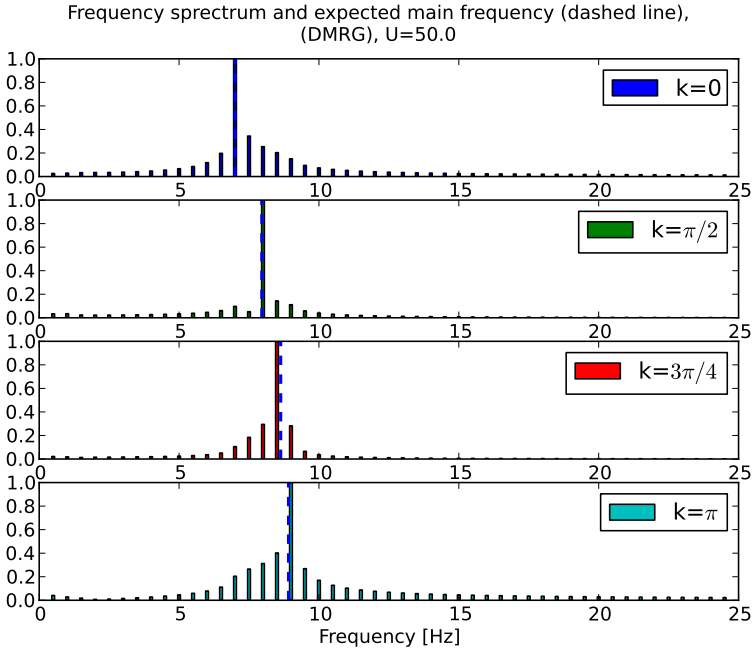

Figure 4.11: Power spectrum of n_k for several momenta. The dashed line indicated the most important frequency expected from perturbation theory, $\omega = U - 6J\cos(k)$ (we take $\bar{n} = 1$). It is very close to the DMRG value. The spectrum shows a different bandwidth for each k.

4.2.2 Influence of the Final Interaction Strength

In figure 4.9, less red areas can be counted as U/J is lowered, indicating smaller frequencies. This can also be seen more precisely in $n_{k=0}$ (figure 4.15). But this is simply due to the lowering of U/J. By contrast, the amplitude grows, indicating larger coherence. But does this result simply in a shift of position in time ? To answer this, we first plot

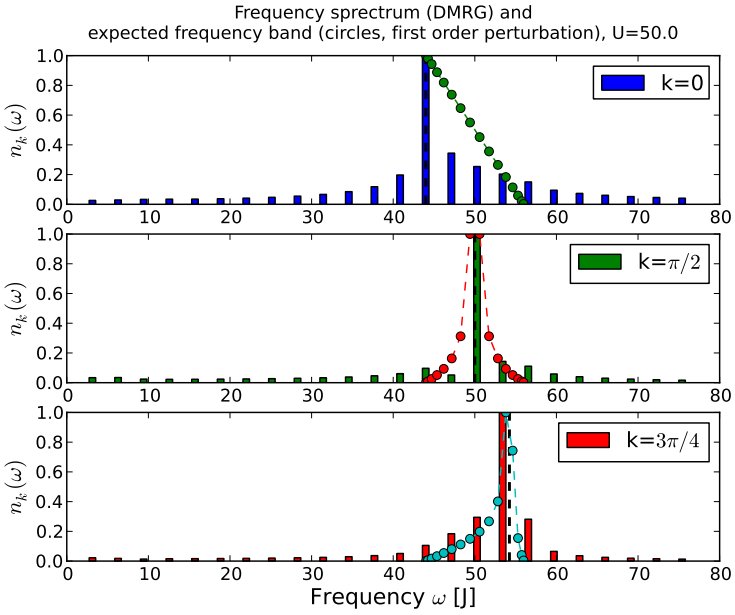

Figure 4.12: Same as before, with the expected bandwidth from perturbation theory (dashed lines). Each frequency is weighted by the factor (4.3). The agreement is qualitatively good with DMRG data (bars), even if slightly underestimated. For $k = 0$, the weight decreases linearly, exponentially for other momenta.

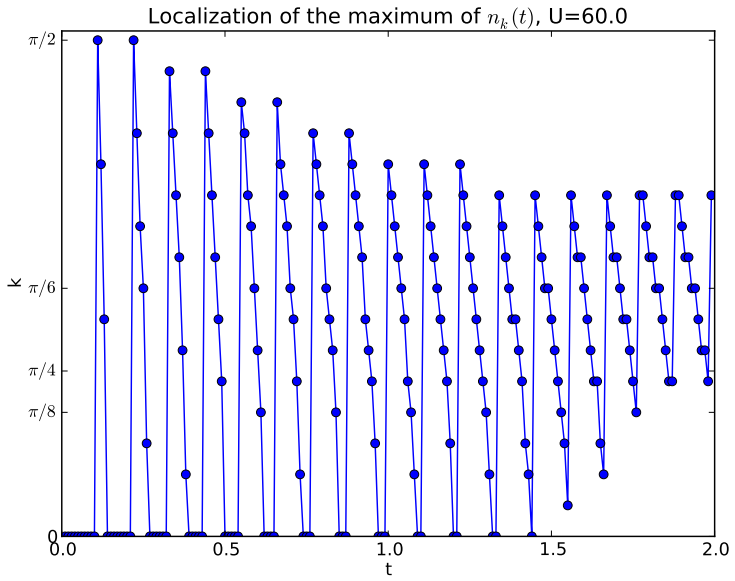

Figure 4.13: Momentum k for which, at time Jt (horizontal axis), the momentum distribution $n_k(t)$ is maximal. Initially, it is $k = 0$, and so is it mostly until $t \approx 0.2J$. But after a period of $2\pi/U$ does $k = \pi/2$ grows in importance. This time is, referring to figure 4.1 (a), roughly when the wavepacket $\langle a_0^\dagger a_2 \rangle$ is reaching a local maximum Afterwards, the maximum is moved around other medium momenta. Note that $k = 0$ continues to compete long after the quasiparticle $\langle a_0^\dagger a_1 \rangle$ has extinguished.

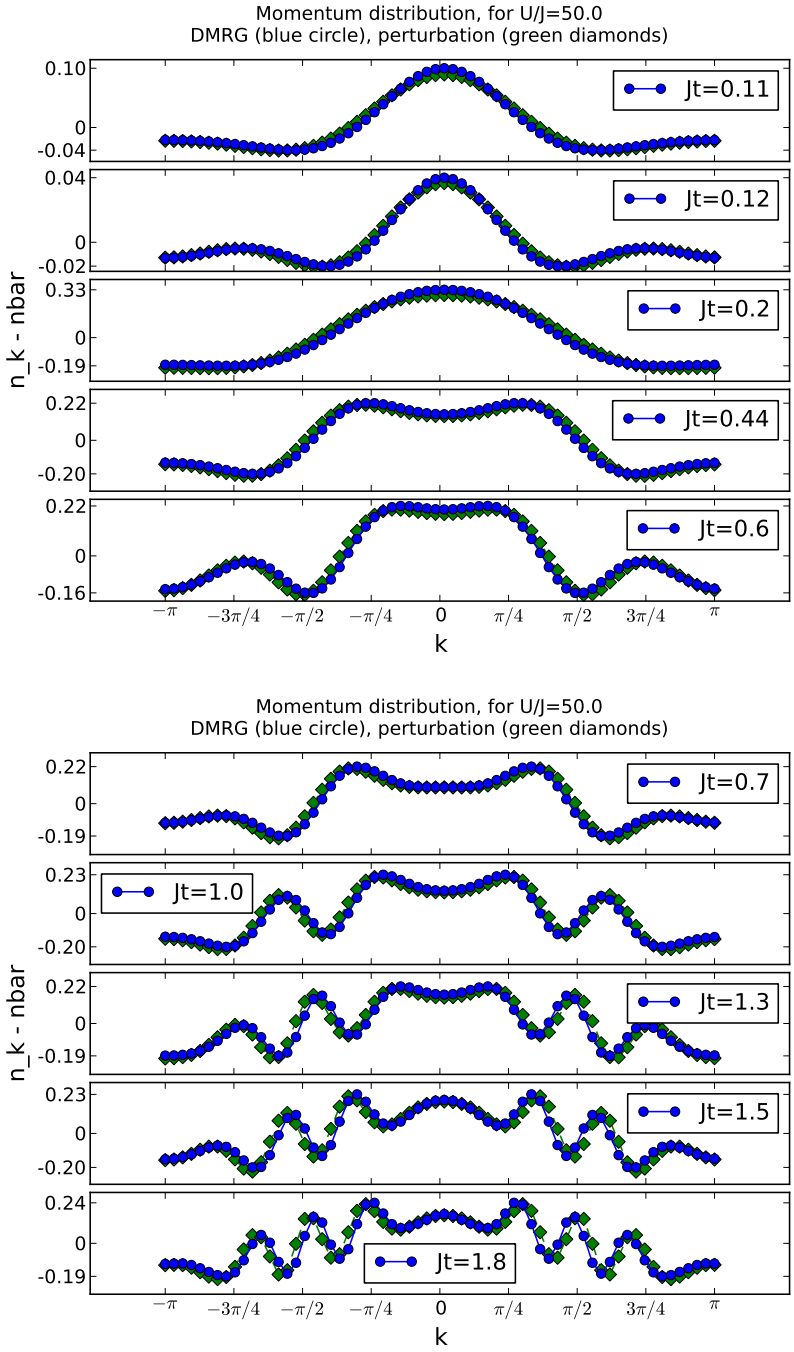

Figure 4.14: Momentum distribution n_k, versus k, at several times. The initial peak at $k = 0$ is progressively transferred to other momentum. More and more local maxima appear as time goes on. The perturbation formula of section 3.2.4 (green diamonds) is in good agreement with the actual DMRG values.

$n_k\,(U, t = m\nu_0(U))$, that is, we compare the momentum distributions at different times, given by $2\pi m/U$. This is shown in 4.16. In (a, $m = 1$), an excellent agreement in found between every cases (we went down to $U/J = 20$, which is still high). This means the difference of U/J does not produce genuinely new effects after one period. This is expected: this time is too short for the bosons to move across the lattice.

Next, comparisons at multiples of ν_0 do not make sense, since it is not the period of oscillation. Instead, we compare the momentum distribution when $n_{k=0}$ reaches a local extrema. This way, we are able to see which momenta is excited when the $k = 0$-component is relaxed. This is shown in picture 4.17. By the third extrema, (b), the difference is clear, and indicates that, with smaller final U/J, higher momenta are excited faster: for $U/J = 60$, three periods are not enough to create the characteristic peak the case $U/J = 20$ shows already well formed and detached from the $k = 0$ region.

Whereas the cases $U/J = 60$ and $U/J = 30$ are mostly comparable, clearly the quasiparticles are propagating faster at $U/J = 30$ and $U/J = 30$, because for the latter additional peaks are already present but nothing of the kind for higher U/J. This complements the observations of the previous section on the propagation velocity. If U/J is further lowered, a new phenomena takes place, which is the subject of the next section.

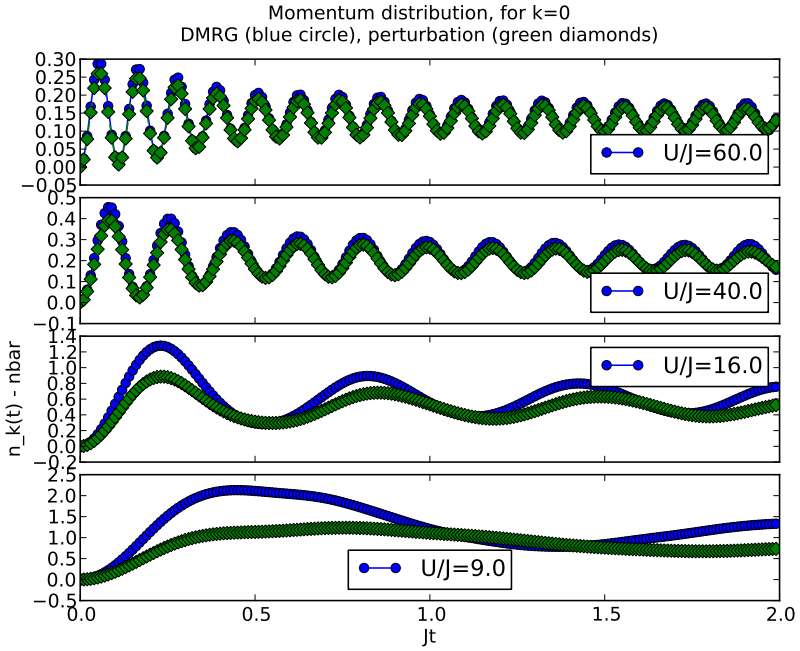

Figure 4.15: Momentum distribution at $k = 0$, versus time, for several values of the final interaction parameter. The wavelength decreases with U/J. At too small U/J, however (see bottom curve, $U/J = 8$), the signal is no more sinusoidal.

4.2.3 Mean Value of the Momentum Distribution

In section 3.2.4, two expressions, particularly simple, were found for $\langle n_{k=0}\rangle$ and $\langle n_{k=\pi/2}\rangle$, with the peculiarity that the latter is a second-order expression. Figure 4.18 (a) presents the DMRG results. To obtain such results, simulations up to times $Jt \approx 4$ have to be

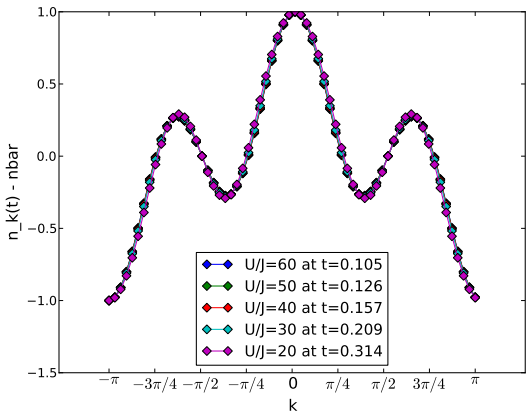

Figure 4.16: Comparison of the momentum distributions, where the comparing time t depends on the interaction strength as $t = 2\pi n/U$, that is, is a multiple of the simplest oscillation frequency arising from the interactions alone.

performed so as to reach steady values. In (b), these formulae are applied in a logarithmic scale (with absolute values). The results deviate considerably for $k = 0$ as soon as $U/J < 15$, but are good for $k = \pi/2$ down to $U/J \approx 10$.

Contributions to $\langle n_k \rangle_t$ mostly stem from the overlap of the perturbed ground state with itself, because all time-dependent part vanished when averaging, and they come from the excited states $|\phi_p\rangle$ (see chapter 3.2.1). Therefore, $\langle n_k \rangle_t$ gives an insight into the steady state the system is reaching, upon which a dynamics of excitations is superimposed and do not relax because of energy conservation. For large U/J, the agreement is excellent for both $k = 0$ and $k = \pi/2$ terms. The growth of the curve when U/J is lowered is well reproduced.

Going toward low U/J, $\langle n_{k=0} \rangle$ grows rapidly, indicating a growth of coherence. The is also shown in figure 4.19, where $\langle n_k \rangle$ is plotted versus k, for several final U/J. The curves approach superfluid shapes, in which state coherence is important. However, this ceases when $U/J \approx 5.5$, where a cross-over takes place. The momentum distribution flattens again. In this regime, the excitations are too strong, and they destroy the coherence. At $U/J = 0$, an exact solution can be derived (see section 3.2.5), and was reported to the figures. It is in continuation of the DMRG data and therefore support the existence of the crossover, which can be interpreted as an effective temperature: the system is heated up permanently to some excited state.

4.3 Conclusion

In this chapter the evolution of an atomic Mott state was investigated. For large final U/J, the evolution is nicely described by perturbation theory. The propagation velocity can be extracted, which is found for high U/J mostly independent of this ratio, in agreement with [9]. In the picture where doublon-hole pairs are considered as propagating quasiparticles, they propagate at a frequency close to U, in a band for which perturbation provides details which remain to be confirmed and understood. During the propagation, coherent

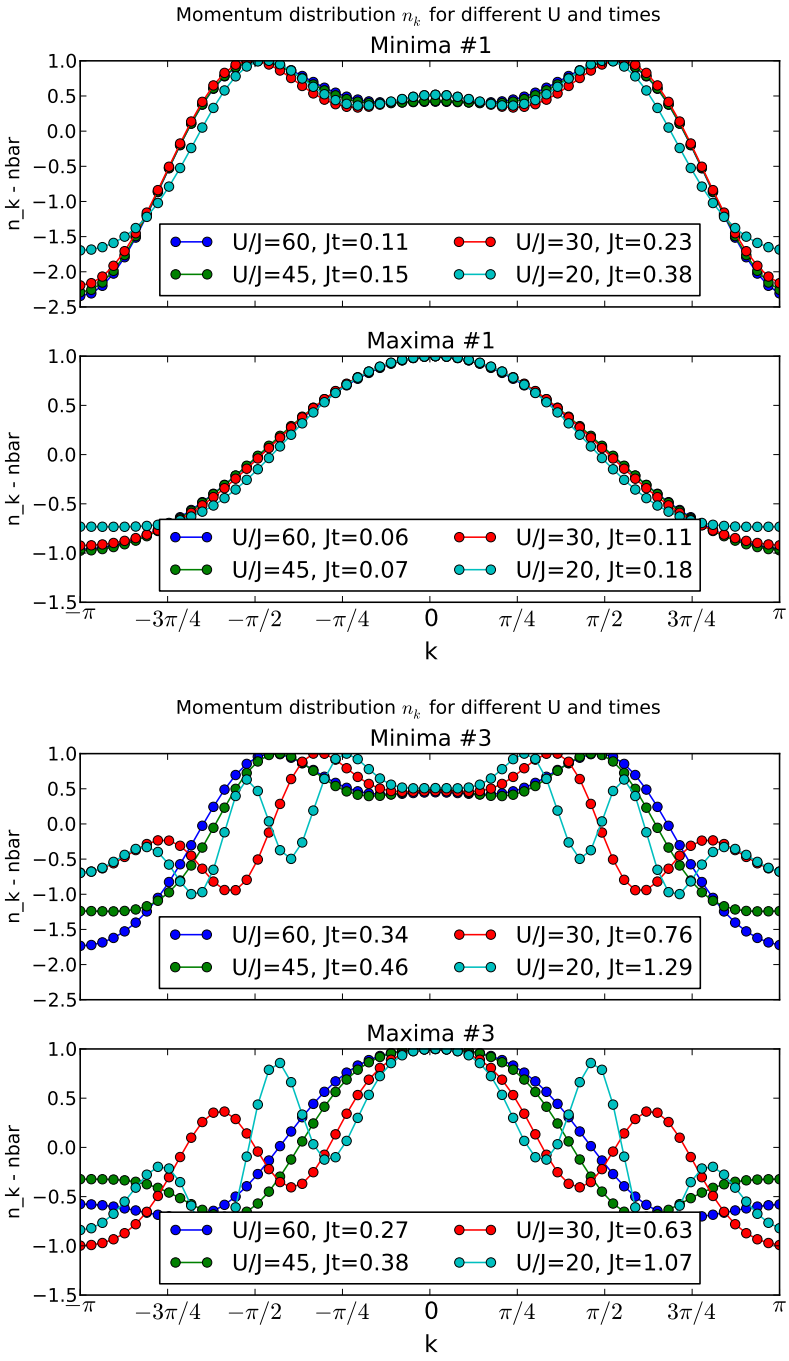

Figure 4.17: Momentum distribution for different U/J, at times when $n_{k=0}$ reaches a minimum (tops) and maximum (bottoms). The corresponding times are indicated in the legend, and every curves are normalized to 1. Whereas few difference are seen in (a), notable differences arises in (b, third extrema). Note that, in (a), the minima are not reached exactly at $2\pi/U$, but slightly after.

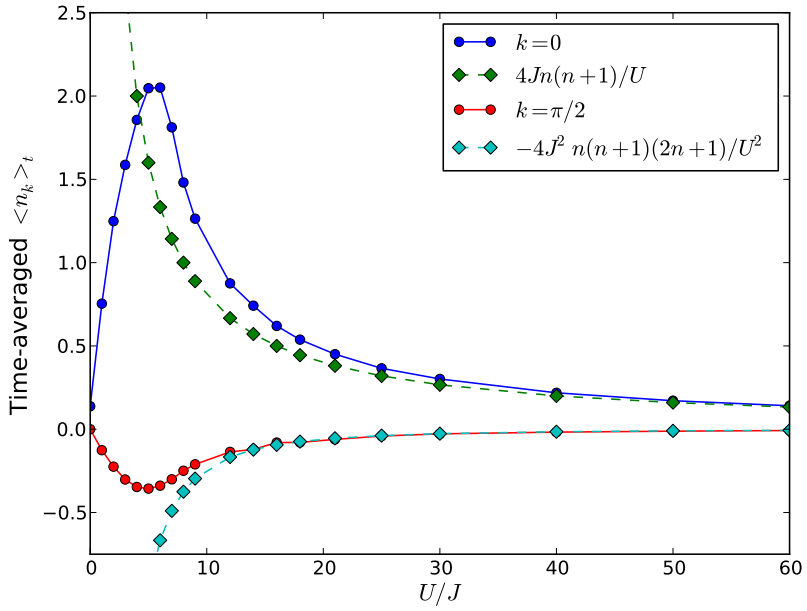

(a)

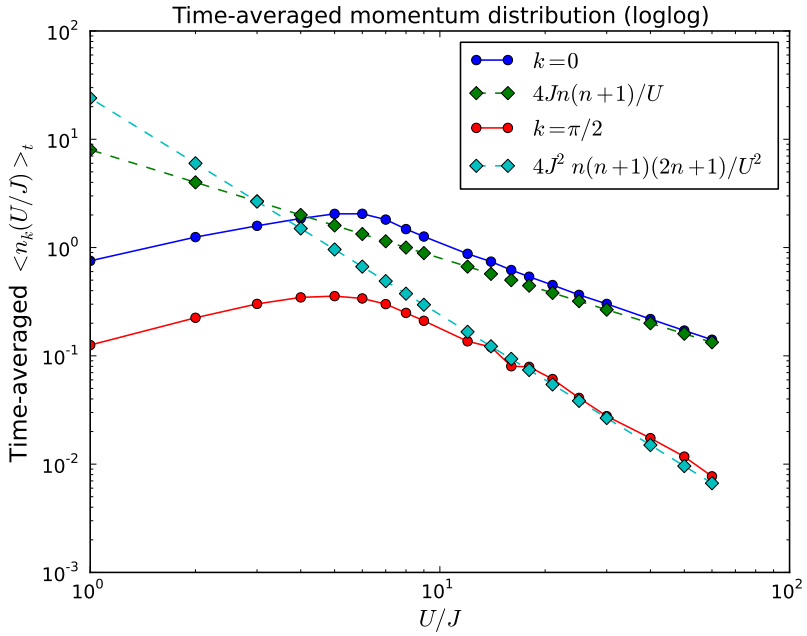

(b)

Figure 4.18: (a) Time-averaged value of the momentum distribution n_k, for $k = 0$ and $k = \pi/2$, versus the final ratio U/J. In (b), the simple results from perturbation theory are compared to DMRG data in a log-log scale. The agreement between DMRG data (plain lines with circle markers) and perturbation theory (dashed lines with diamond markers) is good down to $U/J \approx 5.5$, where a cross-over takes place.

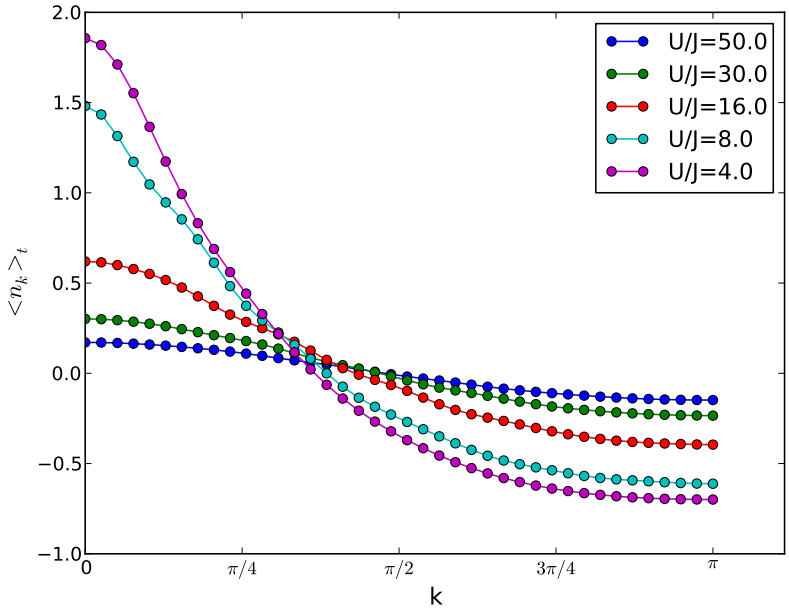

Figure 4.19: Time-averaged momentum distribution versus k, for several final ratio U/J. The growing at small momenta reveals the increase of coherence in the system. However, when U is smaller than approximately 5.5, coherence decreases again (see figure 4.18). Excitations are too strong in this regime and destroy coherence.

superposition of quasiparticles are formed around frequencies $\Omega_k = U - 2J(2\bar{n}+1)\cos(k)$, for momentum k with a non-negligible bandwidth.

But, as U/J decreases, higher band excitations takes more importance and the perturbation theory fails. The coherence continues to grow however, until $U/J \approx 5.5$, where a cross-over to a incoherent state takes place. This is confirmed by the value obtained at $U/J = 0$. Below this point the excitations are too strong and destroy coherence. The quasiparticle picture is invalid, and at approximately the same point it becomes impossible to speak of a propagating signal is the one-body correlation function.

Chapter 5

Dynamics with Mixtures of Bosons

In this final chapter, we study qualitatively the quench of a Mott-insulating state to a low value of U/J in presence of an additional superfluid, and with interactions between the two species. Such mixture can be realized experimentally via state-dependent optical lattices [48]. The two species couple through their density [40, 22]. In our setup, the second species is in a superfluid phase, in which particles move fastly.

However, how this complication quantitatively modifies the behavior of the Mott-insulating state is not clear. Can it be thought as an additional friction in the Mott-insulating species ? Though this interaction induces only tiny modifications in the ground state properties, the time-evolution is different. We find that a propagation signal can still be found in the one-body correlation function and therefore a propagation velocity defined, which decreases when the superfluid is added. In the range of parameter we consider, the quasiparticle picture seems to remain valid, and the added superfluid slows down their spreading. The decoupled case seems to be recovered in the limit of infinite hopping in the added superfluid. Moreover, we give hints in favor of a growth of coherence in the finite coupling case.

5.1 Introduction and Static Properties of Bosonic Mixtures

The Hamiltonian we are considering is:

$$H = H_a + H_b + U_{ab} \sum_i n_{a,i} n_{b,i}, \tag{5.1}$$

where:

$$H_\lambda = -J_\lambda \sum_i (\lambda_i^\dagger \lambda_i + \lambda_{i+1}^\dagger \lambda_i) + \frac{U_\lambda}{2} \sum_i n_{\lambda,i}(n_{\lambda,i} - 1)$$

is the usual Bose-Hubbard Hamiltonian of species λ. Different species are denoted a and b, and their associated annihilation operators at site i are a_i and b_i, their densities $n_{a,i}$ and $n_{b,i}$, respectively. The additional term in the Hamiltonian (5.1) couples the two species via their densities. Though simple in its expression, this new coupling resists mean-field approach [8], in the sense that mean-field fails to predict new phases. Yet, the

ground state of this Hamiltonian is rich and varied [32, 33], exhibiting, beneath Mott-insulating and superfluidity, counter-flow superfluidity and paired superfluidity. On top of superfluidity, charge density waves can exist.

Counter-flow superfluidity takes place at repulsive inter-species interaction $U_{ab}/J_a > 0$ in an incommensurate lattice. Particle-hole pairs are formed (called "anti-pairs" in the literature): a particle in one species bounds with a hole in the other species. On the contrary, in the paired superfluid state, particle-particle pairs are formed. The inter-species interaction U_{ab} has to be attractive (*i.e.* $U_{ab}/J_a < 0$).

However, in the range of parameters we choose, no pairing can be observed. Species a is initially in a Mott-insulating ground state with $U_a/J_a = 40$. Species b is in a superfluid ground state because its filling is 1/2. An additional hardcore constraint is sat on this species, meaning $J_b/U_b = 0$. The hopping J_b/J_a is varied. The inter-species interaction is sat to $U_{ab}/J_a = 4$, the tenth of the ratio U_a/J_a. Below this value, no clear effects on the dynamics can be seen. At the ground state level, for the range $0.5 \leq J_b/J_a \leq 4$ considered, the addition of an inter-species interaction does not modify the one-body correlation functions of a and b above the numerical error, and is therefore completely negligible.

Unlike the single Mott-insulating case, where it is the simple atomic Mott state, in the limit $J_b/J_a \to 0$ the superfluid can not be written down as a product state. Even with the hardcore constraint, it remains a complicated superposition. The superfluid can not be though as "frozen" as would be an integer-filling species, because delocalization remains. However, it will be in some sense "slowed down" to a certain level, in opposition to the large J_b/J_a where delocalization is facilitated. When $J_b/J_a \to 0$, delocalization is not suppressed, only reduced.

In the following sections we investigate the effects of the superfluid on the spreading of correlations in a. To evaluate the influence of b on a (and possibly conversely), U_a/J_a is quenched down to 9, following [9], where such a quench is studied in the single species case. Results are first presented, and discussed in section 5.3, where conjectures on a possible extended quasiparticle picture are formulated.

5.2 Effects of the Superfluid on the Time-evolution

5.2.1 One-body Correlations and Propagation Velocity

Our aim is to investigate the effects of the parameter J_b/J_a which controls the kinetic energy of the superfluid. Figure 5.1 presents the time-evolution of the correlations functions of both species. The blue curve is the single-species results, obtained therefore with $U_{ab} = 0$. It serves as a witness. Such curves were discussed in the previous chapter; although there we had initially $J_a/U_a = 0$, the situation is mostly comparable.

The propagating signal is preserved. A notable thing is the lowering of the correlations in b, which are stronger for small J_b/J_a. The case $J_b/J_a = 4$ (purple curves) is the closest to the $U_{ab}/J_a = 0$ situation, in both $\langle a_0^\dagger a_d \rangle$ and $\langle b_0^\dagger b_d \rangle$. This implies the superfluid mainly act as a friction in a.

In the quenched Mott-insulating state, the dynamics is different. As the green curves of the top panels of 5.1 (a) and (b), for which $J_b/J_a = 1$ is small, show, the peak is flattened, and it becomes difficult to localize clearly a maximum. This broadening

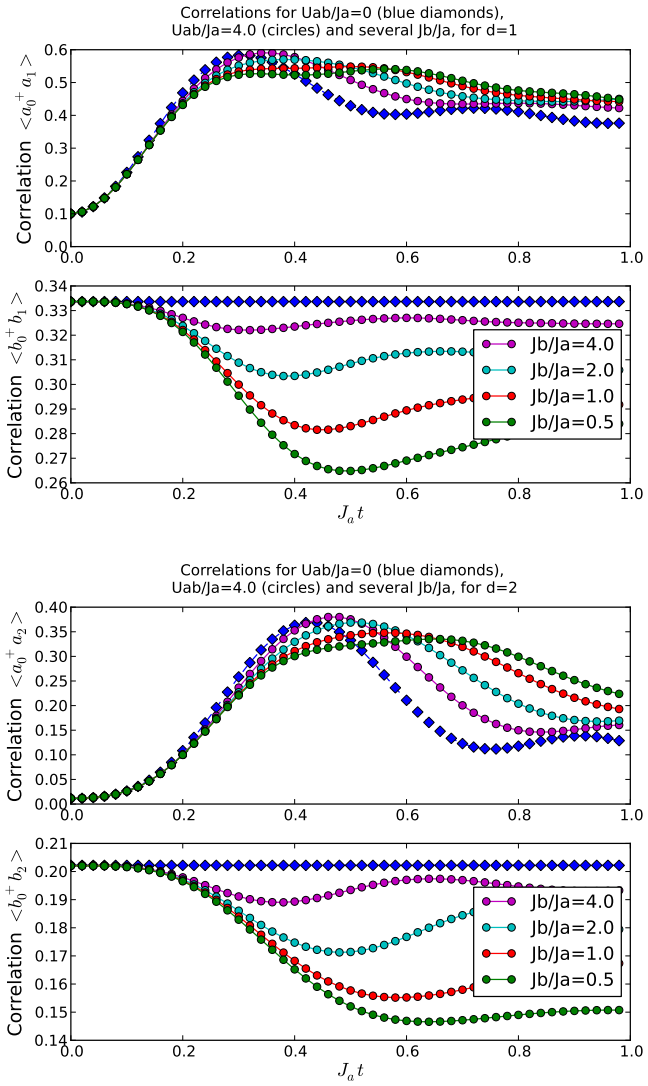

Figure 5.1: One-body correlation functions for the quenched Mott-insulating state ($\langle a_0^\dagger a_d \rangle$, tops) and the superfluid state ($\langle b_0^\dagger b_d \rangle$, bottoms), for (a) $d = 1$ and (b) $d = 2$. Each curve is for a different J_b, except the blue lines with diamond markers, for which $U_{ab} = 0$ (the single species case). At short times ($J_a t < 0.1$), no effects can be seen. Whereas in the quenched Mott-insulating state a propagating signal can be identified, in the superfluid the one-body correlations decrease to a plateau and show small oscillations around a steady values. This indicates that quasiparticles are formed in the Mott-insulator, but not in the superfluid.

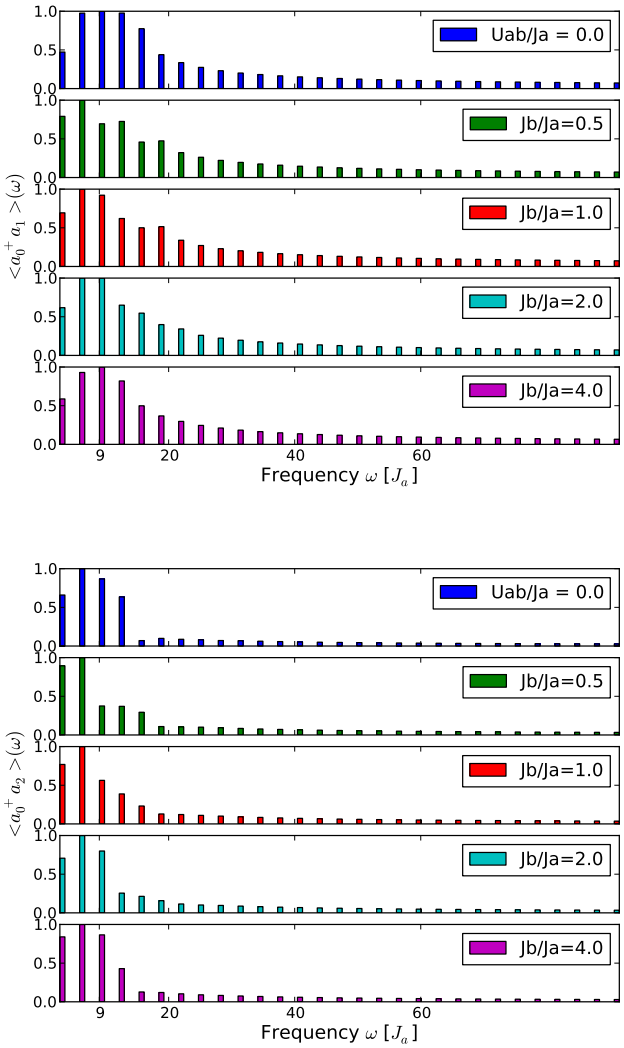

Figure 5.2: Fourier transform of the one-body correlation function, (a) $\langle a_0^\dagger a_1 \rangle$ and (b) $\langle a_0^\dagger a_2 \rangle$ of the Mott-insulating species. Whereas in the single-species cases ($U_{ab}/J_a = 0$) the main frequency is close to the final U_a/J_a, it appears shifted for small J_b/J_a toward lower values. This is why, on figure 5.1, the maxima is observed at later times. When J_b/J_a is higher, the main frequency moves toward the single-species one, $U_a/J_a \approx 9$. Moreover, the superfluid modifies the spectrum. Smaller frequencies carry more weight whereas large frequencies are deprecated. For large J_b/J_a the single-species Fourier transform seems to be recovered (see the proximity between the purple and blue bars).

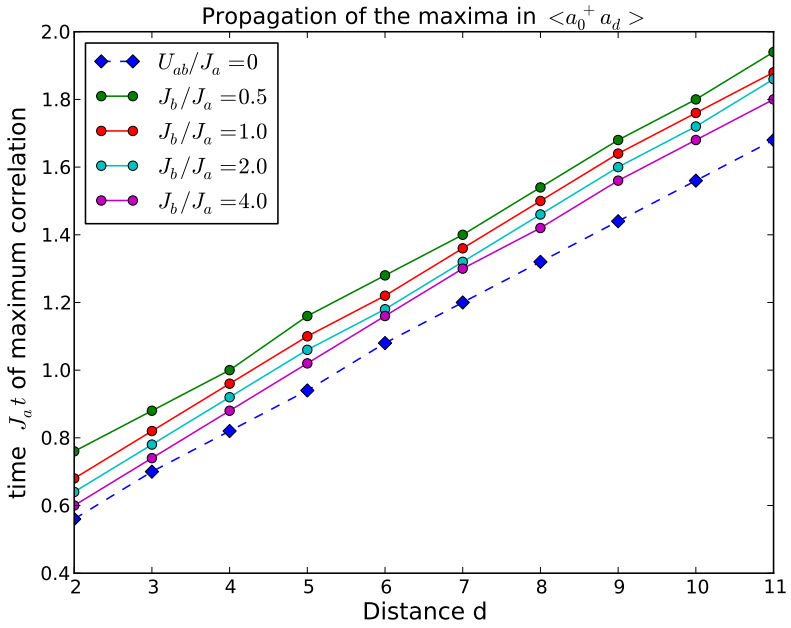

Figure 5.3: Propagation of correlations in the presence of a superfluid component: times for which $\langle a_0^\dagger a_d \rangle$ is maximal. When $U_{ab}/J_b \neq 0$, the positions are shifted toward larger times, indicating a delay, but the curves remain qualitatively linear, allowing in principle to extract a velocity.

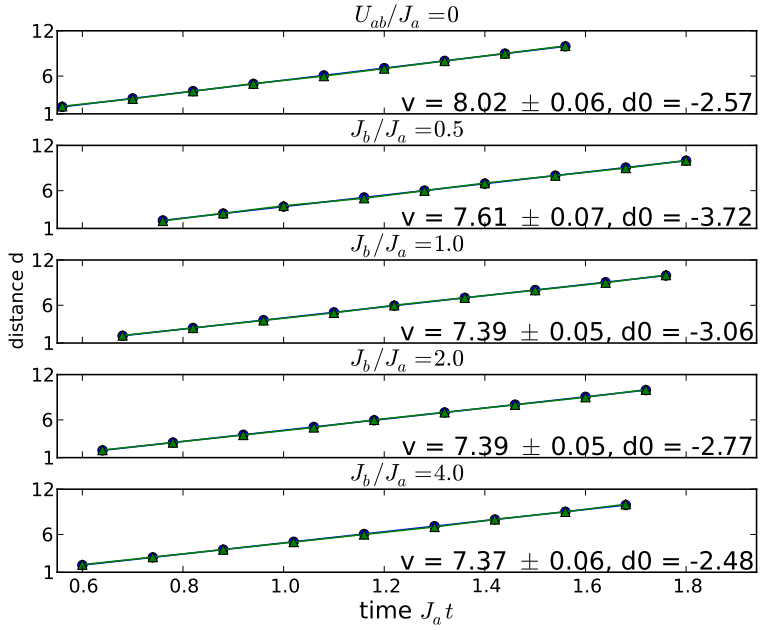

Figure 5.4: Fits of the velocity of the propagating quasiparticle, with $d = vt + d_0$. The velocities v are in units of J_a. The error is the standard error from the linear regression procedure. The given values should be taken with care, as noticed in the text. The velocities are clearly smaller in the case $U_{ab}/J_b \neq 0$ presented.

indicates slower propagation, that is, with smaller frequencies, as figure 5.2 shows. In this figure is plotted the Fourier transform of the signals of figure 5.1. A shift of frequencies toward values lower than $\omega \approx U_a/J_a = 9$ can be observed as well as the suppression of higher frequencies. However, as J_b/J_a is increased, the Fourier transform of the single-species case is approximately recovered.

This can also be seen in 5.3, which shows the times for which correlations hit a maxima. Propagation seems to remain linear. However, it is difficult to say how the velocity is modified. As we already noticed, for low J_b/J_a, the broadening of the one-body correlation function makes it difficult to find a true maximum. Figure 5.4 indicates a velocity which decreases with increasing J_b/J_a, until $J_b \approx U_{ab}$. This confirms the previous results: the propagation is slowed down by the superfluid, except in the cases $U_{ab}/J_b = 0$. However, the actual velocities obtained from our fits should be taken with care, because the one-body correlation function does not show a clear maxima when $J_b/J_a < 2$ (see green and red curves of 5.1 (a) and (b) top). This is why our results are only indications of a tendency which remains to be demonstrated experimentally.

5.2.2 Momentum Distribution and Coherence

In the previous chapter and for a initial single Mott atomic state, the coherence grew after the quench for $U_a/J_a > 5.5$. For mixtures, the one-body correlation function of the quenched Mott insulator also shows a propagating signal, but, for low J_b/J_a, the signal is broader. How is the coherence enhancement modified ? To answer, we study the momentum distribution $n_k(t) - \bar{n}_a$ of species a, the Mott insulator. It is plotted in figure 5.5 for several momenta. As in the previous section for $\langle a_0^\dagger a_d \rangle$, the frequencies are lower for small J_a/J_b, and approach the case $U_{ab}/J_b = 0$ as J_a/J_b grows. This fact is also supported by the Fourier transform, see figure 5.6 for an example with $k = 3\pi/4$.

What is more interesting is the fact that $n_{k=0}(t)$ is actually larger in amplitude when $U_{ab}/J_a \neq 0$, at least in the range J_b/J_a presented. This indicates a growth of coherence on the presented time-scales. It can also be seen in the Fourier transform, figure 5.6: for $J_b/J_a < 4$, although the bandwidths are not larger, more frequencies appear, and they carry more weight. Thus, more modes are coherently superposed when a superfluid is present. As J_b/J_a is increased, the situation must tend toward the blue line, $U_{ab}/J_a = 0$, because it is a particular case of $U_{ab}/J_b = 0$, and therefore coherence decreases.

5.3 Discussion and Conclusion

As in the single-species case, a propagating signal can be seen in the one-body correlations. By looking at the maxima of this signal, the propagation is approximately linear, and a velocity can be extracted. This supports the transposition of the quasiparticle picture to mixtures at non-zero and finite U_{ab}/J_b. However, the signal is also found flatter and the error in the velocity determination larger.

With a slower signal, the times-scales which should be reached to gain a correct insight into the dynamics are larger. In particular, for the momentum distribution, the growth of coherence we saw for $J_a t < 2$ might not reflect the long-standing behavior of the system,

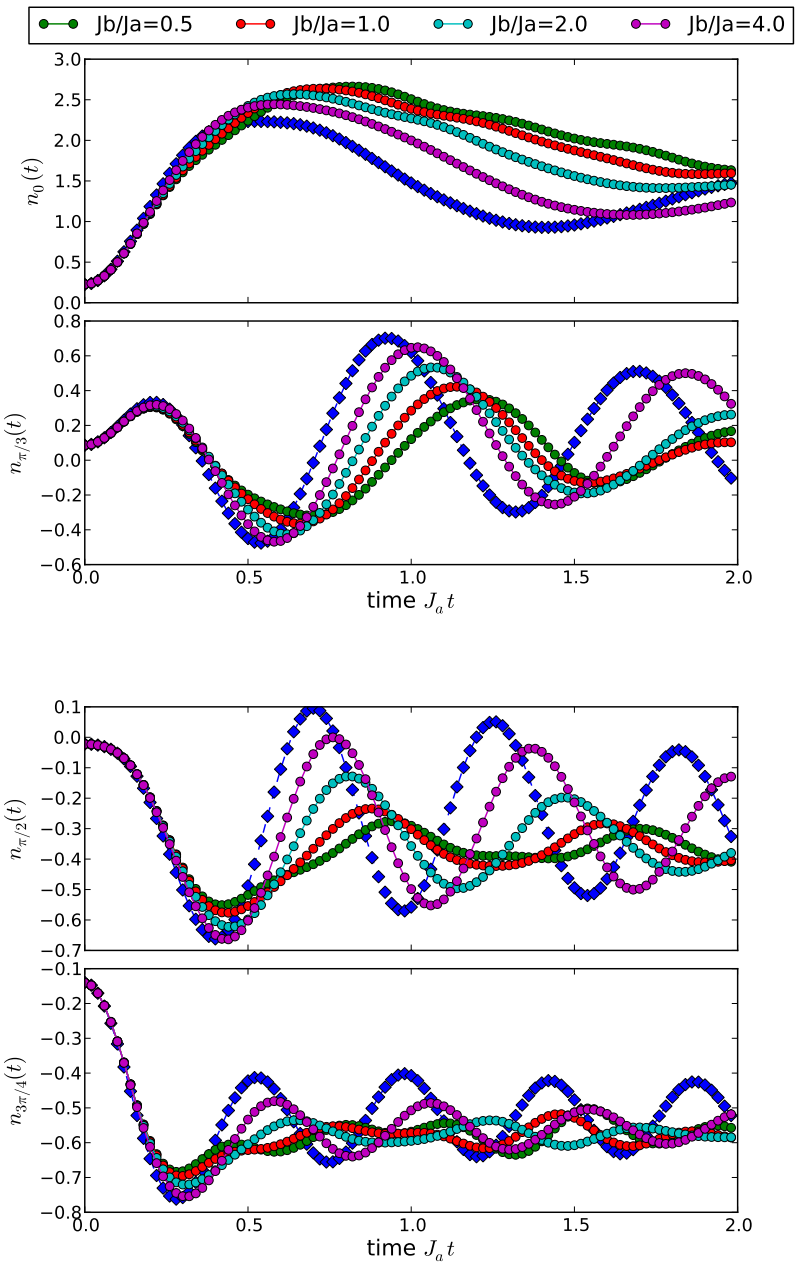

Figure 5.5: Momentum distribution $n_k(t) - \bar{n}_a$ of species a, for, from top to bottom, $k = 0$, $k = \pi/2$, $k = \pi/3$ and $k = 3\pi/4$. As usual the blue line with diamond markers is the case $U_{ab}/J_b = 0$. Unlike the other momenta, for $k = 0$ the momentum distribution is larger. Although the long-time behavior might be different, on this time-scale a growth of coherence can be seen.

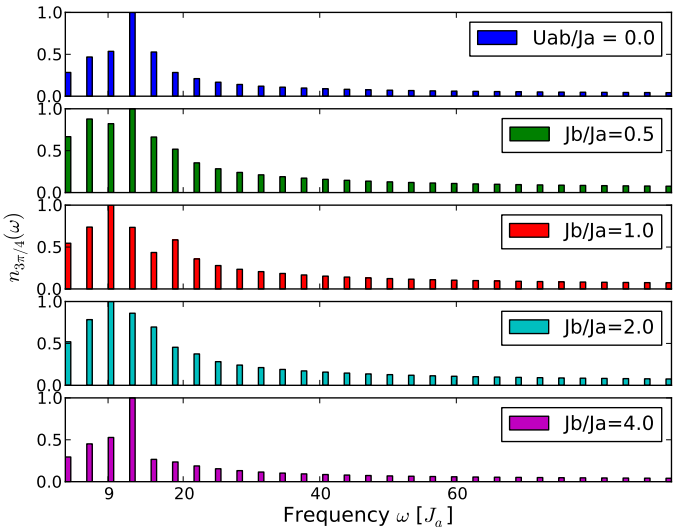

Figure 5.6: Example of the fourier transform of the momentum distribution of the Mott insulating state, $n_k(\omega)$, for $k = 3\pi/4$. A broadening can be seen when $U_{ab}/J_a \neq 0$. As for $\langle a_0^\dagger a_d \rangle$ (see figure 5.2), the Fourier transform for $J_b/J_a = 4$ (bottom) is the closest to the case $U_{ab}/J_a = 0$. The same phenomena are observed for all other momenta.

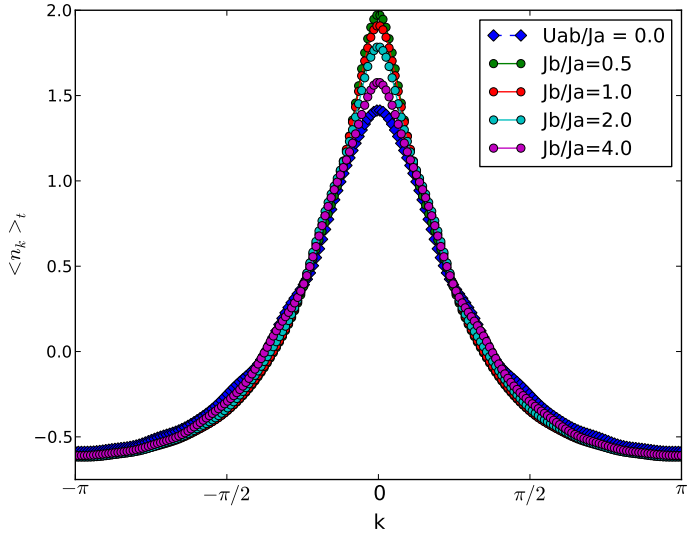

Figure 5.7: Time-averaged momentum distribution, versus momentum k, for different final J_b/J_a, and the witness $U_{ab}/J_a = 0$ in blue. This is the average of the DMRG data on the range $0 < J_a t < 2.0$, which is, for $k \approx 0$, too small to obtain true steady values. Therefore, this curve is only a hint which might indicate a growth of coherence when $U_{ab}/J_b \neq 0$. This growth can be interpreted as the contribution of the superfluid: the two species are interacting coherently. Small J_a/J_b results in higher coherence, because the quasiparticle of figure 5.1 is broader, and have therefore more time to interact. This can be interpreted as a dressing of the quasiparticle.

but is gives an indication: whereas for other momenta n_k is not modified in average (see figure 5.7 and the legend), for $k = 0$ (and close to 0) the momentum distribution is larger.

In the single-species case, a cross-over was observed at some low final U_a/J_a, where coherence was destroyed (see chapter 4.2.3). This also corresponds approximately to the point where the quasiparticle picture failed, because no propagation could be seen in the one-body correlation function. Therefore, if this additional coherence is confirmed, it would be a firm indication that the quasiparticle picture can be transposed to mixtures.

Physically, this would mean the Mott quasiparticles are dressed by the superfluid, traveling slower, but with additional frequencies. As the figure 5.6 indicates, the quasiparticles have a broader and higher power spectrum. Though slower, they are not destroyed by the superfluid, but they have more time to interact and carry a more complex structure, something one could not infer from the broadening of $\langle a_0^\dagger a_d \rangle$ alone. One the contrary the less well-defined maxima could have been interpreted as the destruction of the quasiparticle, which does not seem to be the case.

However, it not clear how the situation will evolve if U_{ab}/J_a is larger. We considered the case $U_{a,\text{initial}}/U_{ab} = 10$, and therefore the superfluid could almost be treated as a perturbation. As mentioned in the introduction, the ground state will be modified when $U_{ab} \sim U_a$ by the formation of bound particle/particle pairs or particle/hole pairs. Such pairs do not necessarily increase coherence, because the interaction between these pairs might be destructive. We also performed simulations with $U_{a,\text{initial}}/U_{ab} = 5$, so closer to the non-perturbative regime, but with the same ground state, and a similar growth of coherence was observed. The same proviso on the time-scale applies. In contrast, a propagation velocity became more complicated to find. It is therefore not clear whether the quasiparticle picture will stand when $U_{ab} \sim U_{a,\text{initial}}$.

In conclusion, though further studies are necessary to confirm our tendency, the addition of a superfluid seems to result in a growth of coherence, and not in the destabilization of the Mott state. The picture of a propagating quasiparticle developed in [9] may remain applicable even at larger $U_{ab}/U_{a,\text{initial}}$, although the signal in the one-body correlation function might not be convincing. The growth of coherence, which can be seen in the momentum distribution, may serves as an indication.

At small $U_{ab}/U_{a,\text{initial}}$, a dressed quasiparticle theory should be enough to describe the physics. On the numerical side, more systematic exploration of the parameter space, spanned by U_{ab}/J_b, should be led. DMRG is adapted to this end, even if the limit $J_b/U_{ab} \to 0$ is also very hard to simulate. From both points of view, the space is open for improvements and new methods.

Chapter 6

Conclusion

In this work we studied the time-evolution of a Mott-insulating state in one dimension when quenched to a lower interaction strength. Mott-insulating states are obtained with a strongly interacting cold atomic cloud loaded in an optical lattice, a setup which is experimentally common nowadays. Though we adopted a numerical point of view, the physical quantities we studies are accessible experimentally, and our results are ready for experimental confrontations. In particular, we used the momentum distribution, which can be measured by time-of-flight measurements. It provides a fascinating insight into the quantum many-body physics at work.

In particular, the momentum distribution gives information about the coherence in the system. Whereas the atomic Mott state, which is obtained by taking the interactions to infinity, presents no coherence, after the quench, coherence appear and do persist. To interpret this phenomena, the picture of propagating quasiparticles was developed in [9]. They transports correlation with a finite velocity, which depends on the final ratio U/J.

A dynamics between quasiparticles takes place. In chapter 4, we showed they are superposed coherently in time. The simplest first-order perturbation theory catches the main structure of the evolution down to $U/J \approx 10$, in agreement with more sophisticated approaches such as the one developed in [4].

Below, the naive picture in which a particle is removed from site i and placed on site $i+1$ after the quench is not correct anymore. At some $U/J \approx 5.5$, a crossover takes place: as if an effective temperature was raised, excitations become too strong and destabilize the system, destroying coherence. So far no theoretical model can describe this phenomenon.

Similarly, to our knowledge no theoretical predictions of the behavior of the quenched Mott-insulating state in interaction with an additional superfluid exist. In our intuition, for the range of parameter considered, the quasiparticles picture is still valid, and the superfluid increases their coherence. Our results suggest that a dressed quasiparticle picture might prove useful when U_a/U_{ab} is small enough.

What happens in the limit of small U_{ab}/J_b remains open. In future works, numerical simulations have to be optimized for the treatment of mixtures at strong J_b/U_{ab}, along with the development of a new theoretical approach, for example based on a dressed quasiparticle.

Bibliography

[1] M. H. Anderson, J. R. Ensher, M. R. Matthews, C.E. Wieman, and E. A. cornell. Observation of Bose-Einstein condensation in a dilute atomic vapor. *Science*, 269(5221):198–201, 1995.

[2] M. R. Andrews, C. G. Townsend, H. J. Miesner, D. S. Durfee, D. M. Kurn, and W. Ketterle. Observation of interference between two Bose condensates. *Science*, 275(5300):637–641, 1997.

[3] L.E. Ballentine. *Quantum Mechanics: A Modern Development*. World Scientific, 1998.

[4] P. Barmettler, D. Poletti, M. Cheneau, and C. Kollath. Propagation front of correlations in an interacting Bose gas. *Phys. Rev. A*, 85:053625, 2012.

[5] I. Bloch and A. Rosch. Exploring strongly correlated quantum many-body systems with ultracold atoms in optical lattices. *Phys. Status Solidi B*, 247(3):530–536, 2010.

[6] C. C. Bradley, C. A. Sackett, J. J. Tollett, and R. G. Hulet. Evidence of Bose-Einstein condensation in an atomic gas with attractive interactions. *Phys. Rev. Lett.*, 75:1687–1690, 1995.

[7] M. A. Cazalilla and J. B. Marston. Time-dependent density-matrix renormalization group: A systematic method for the study of quantum many-body out-of-equilibrium systems. *Phys. Rev. Lett.*, 88:256403, 2002.

[8] G.-H. Chen and Y.-S. Wu. Quantum phase transition in a multicomponent Bose-Einstein condensate in optical lattices. *Phys. Rev. A*, 67:013606, 2003.

[9] M. Cheneau, P. Barmettler, D. Poletti, M. Endres, P. Schauss, T. Fukuhara, C. Gross, I. Bloch, C. Kollath, and S. Kuhr. Light-cone-like spreading of correlations in a quantum many-body system. *Nature*, 481(7382):484–487, 2012.

[10] S. L. Cornish, N. R. Claussen, J. L. Roberts, E. A. Cornell, and C. E. Wieman. Stable ^{85}Rb Bose-Einstein condensates with widely tunable Interactions. *Phys. Rev. Lett.*, 85:1795–1798, 2000.

[11] F. Dalfovo, S. Giorgini, L. P. Pitaevskii, and S. Stringari. Theory of Bose-Einstein condensation in trapped gases. *Rev. Mod. Phys.*, 71(3):463–512, 1999.

[12] K. B. Davis, M.-O. Mewes, M. A. Joffe, M. R. Andrews, and W. Ketterle. Evaporative cooling of sodium atoms. *Phys. Rev. Lett.*, 74:5202–5205, 1995.

[13] E. A. Donley, N. R. Claussen, S. L. Cornish, J. L. Roberts, E. A. Cornell, and C. E. Wieman. Dynamics of collapsing and exploding Bose-Einstein condensates. *Nature*, 412(6844):295–299, 2001.

[14] N. Elstner and H. Monien. Dynamics and thermodynamics of the Bose-Hubbard model. *Phys. Rev. B*, 59:12184–12187, 1999.

[15] M. P. A. Fisher, P. B. Weichman, G. Grinstein, and D. S. Fisher. Boson localization and the superfluid-insulator transition. *Phys. Rev. B*, 40:546–570, 1989.

[16] A. Flesch, M. Cramer, I. P. McCulloch, U. Schollwöck, and J. Eisert. Probing local relaxation of cold atoms in optical superlattices. *Phys. Rev. A*, 78:033608, 2008.

[17] T. Giamarchi. *Quantum Physics in One Dimension*. International Series of Monographs on Physics. Clarendon, 2004.

[18] D. Gobert, C. Kollath, U. Schollwöck, and G. Schütz. Real-time dynamics in spin-1/2 chains with adaptive time-dependent density matrix renormalization group. *Phys. Rev. E*, 71:036102, Mar 2005.

[19] M. Greiner. *Ultracold quantum gases in three-dimensional optical lattice potentials*. Ludwig-Maximilians-Universität München, 2003.

[20] M. Greiner, O. Mandel, T. Esslinger, T. W. Hansch, and I. Bloch. Quantum phase transition from a superfluid to a Mott insulator in a gas of ultracold atoms. *Nature*, 415(6867):39–44, 2002.

[21] R. Grimm, M. Weidemuller, and Y. B. Ovchinnikov. Optical dipole traps for neutral atoms. volume 42 of *Advances in Atomic, Molecular and Optical Physics*, pages 95–170. Academic Press Inc., 2000.

[22] Z. Hadzibabic, C. A. Stan, K. Dieckmann, S. Gupta, M. W. Zwierlein, A. Görlitz, and W. Ketterle. Two-Species mixture of quantum degenerate Bose and Fermi gases. *Phys. Rev. Lett.*, 88:160401, 2002.

[23] D. Jaksch, C. Bruder, J. I. Cirac, C. W. Gardiner, and P. Zoller. Cold bosonic atoms in optical lattices. *Phys. Rev. Lett.*, 81:3108–3111, 1998.

[24] D. Jaksch and S.A. Clark. *Cold Atoms in Optical Lattices*. Springer, 2012.

[25] T. D. Kühner. *Dynamics with the Density Matrix Renormalization Group*. Rheinischen Friedrich-Wilhelms Universität Bonn, 1999.

[26] T. D. Kühner and H. Monien. Phases of the one-dimensional Bose-Hubbard model. *Phys. Rev. B*, 58(22):14741–14744, 1998.

[27] C. Kittel. *Introduction To Solid State Physics*. Wiley, 2005.

[28] C. Kollath. *The adaptive time-dependent density-matrix renormalization-group methode: development and applications*. Technischen Hochschule Aachen, 2005.

[29] C. Kollath, A. M. Läuchli, and E. Altman. Quench dynamics and nonequilibrium phase diagram of the Bose-Hubbard model. *Phys. Rev. Lett.*, 98:180601, Apr 2007.

[30] T. D. Kühner and S. R. White. Dynamical correlation functions using the density matrix renormalization group. *Phys. Rev. B*, 60:335–343, 1999.

[31] T. D. Kühner, S. R. White, and H. Monien. One-dimensional Bose-Hubbard model with nearest-neighbor interaction. *Phys. Rev. B*, 61:12474–12489, 2000.

[32] A. Kuklov, N. Prokof'ev, and B. Svistunov. Commensurate two-component bosons in an optical lattice: Ground state phase diagram. *Phys. Rev. Lett.*, 92:050402, 2004.

[33] A. B. Kuklov and B. V. Svistunov. Counterflow superfluidity of two-species ultracold atoms in a commensurate optical lattice. *Phys. Rev. Lett.*, 90:100401, 2003.

[34] C. Lanczos. An iteration method for the solution of the eigenvalue problem of linear differential and integral operators. *J. Res. Natl. Bur. Stand.*, 45:255–282, 1950.

[35] E. H. Lieb and D. W. Robinson. The finite group velocity of quantum spin systems. *Comm. Math. Phys.*, 28(3):251–257, 1972.

[36] A. Läuchli and C. Kollath. Spreading of correlations and entanglement after a quench in the one-dimensional Bose-Hubbard model. *Journ. Stat. Mech.*, 2008.

[37] M. A. Cazalilla. Low-energy properties of a one-dimensional system of interacting bosons with boundaries. *Europhys. Lett.*, 59(6):793–799, 2002.

[38] S. Masuo. Relationship between d-dimensional quantal spin systems and $(d+1)$-simensional Ising systems. *Progress of Theoretical Physics*, 56(5):1454–1469, 1976.

[39] S. Masuo. General theory of fractal path integrals with applications to many-body theories and statistical physics. *J. Math. Phys.*, 32(400), 1991.

[40] T. Mishra, R. V. Pai, and B. P. Das. Phase separation in a two-species Bose mixture. *Phys. Rev. A*, 76:013604, 2007.

[41] A. Peres. *Quantum Theory: Concepts and Methods.* Fundamental Theories of Physics. Kluwer Academic Publishers, 1995.

[42] C. J. Pethick and H. Smith. *Bose-Einstein Condensation in Dilute Gases.* Cambridge University Press, 2002.

[43] P. Pippan, H. G. Evertz, and M. Hohenadler. Excitation spectra of strongly correlated lattice bosons and polaritons. *Phys. Rev. A*, 80:033612, 2009.

[44] R. Roth and K. Burnett. Superfluidity and interference pattern of ultracold bosons in optical lattices. *Phys. Rev. A*, 67:031602, 2003.

[45] U. Schollwöck. The density-matrix renormalization group. *Rev. Mod. Phys.*, 77:259–315, 2005.

[46] U. Schollwöck. The density-matrix renormalization group in the age of matrix product states. *Annals of Physics*, 326(1):96–192, 2011.

[47] J. Sirker and A. Klümper. Real-time dynamics at finite temperature by the density-matrix renormalization group: A path-integral approach. *Phys. Rev. B*, 71:241101, 2005.

[48] P. Soltan-Panahi, J. Struck, P. Hauke, A. Bick, W. Plenkers, G. Meineke, C. Becker, P. Windpassinger, M. Lewenstein, and K. Sengstock. Multi-component quantum gases in spin-dependent hexagonal lattices. *Nat. Phys.*, 7:434–440, 2011.

[49] L.N. Trefethen and D. Bau. *Numerical Linear Algebra*. Miscellaneous Bks. Society for Industrial and Applied Mathematics, 1997.

[50] F. Verstraete and J. I. Cirac. Matrix product states represent ground states faithfully. *Phys. Rev. B*, 73:094423, 2006.

[51] G. Vidal. Efficient classical simulation of slightly entangled quantum computations. *Phys. Rev. Lett.*, 91:147902, 2003.

[52] S. R. White. Density matrix formulation for quantum renormalization groups. *Phys. Rev. Lett.*, 69:2863–2866, 1992.

[53] S. R. White. Density matrix renormalization group algorithms with a single center site. *Phys. Rev. B*, 72:180403, 2005.